



ESA/Contract No. 4000126561/19/I-NB

Consortium Members



ESA Sea Level CCI+

# Algorithm Theoretical Basis Document

Reference:

Nomenclature: SLCCI+\_ATBD\_007\_AlgorithmTheoreticalBasisDoc

Issue: 1.2


Date: Oct. 1, 20




**Chronology Issues:**

Issue:	Date:	Reason for change:	Author
1.0	30/09/19	Initial Version	F. Birol (LEGOS), M. Passaro (TUM)
1.1	07/01/20	Updated after review comments from ESA	JF Legeais, F. Birol
1.2	01/10/20	Integration of Jason-3, Envisat and SARAL in the production system	F. Nino, F. Birol (LEGOS)

**People involved in this issue:**

Written by:	F. Birol (LEGOS), M. Passaro (TUM),		
Checked by:	JF Legeais (CLS)		
Approved by:	JF Legeais (CLS)	02/10/2020	

**Acceptance of this deliverable document:**

Accepted by ESA:	J. Benveniste (ESA)	06/10/2020	
------------------	---------------------	------------	---

**Distribution:**

Company	Names	Contact Details
ESA	J. Benveniste A. Ambrozio, M. Restano	<a href="mailto:Jerome.Benveniste@esa.int">Jerome.Benveniste@esa.int</a> ; <a href="mailto:Americo.Ambrozio@esa.int">Americo.Ambrozio@esa.int</a> ; <a href="mailto:Marco.Restano@esa.int">Marco.Restano@esa.int</a>
CLS	J.-F. Legeais ; P. Prandi ; S. Labroue ; M. Lievin ; A. Guerrou	<a href="mailto:jlegeais@groupcls.com">jlegeais@groupcls.com</a> ; <a href="mailto:pprandi@groupcls.com">pprandi@groupcls.com</a> ; <a href="mailto:slabroue@groupcls.com">slabroue@groupcls.com</a> ; <a href="mailto:mlievin@groupcls.com">mlievin@groupcls.com</a> ; <a href="mailto:aguerrou@groupcls.com">aguerrou@groupcls.com</a> ;
LEGOS	A. Cazenave ; B. Meyssignac ; F. Birol; F. Nino; F. Leger; Y. Gouzenes	<a href="mailto:anny.cazenave@legos.obs-mip.fr">anny.cazenave@legos.obs-mip.fr</a> ; <a href="mailto:Benoit.Meyssignac@legos.obs-mip.fr">Benoit.Meyssignac@legos.obs-mip.fr</a> ; <a href="mailto:florence.birol@legos.obs-mip.fr">florence.birol@legos.obs-mip.fr</a> ; <a href="mailto:fernando.nino@legos.obs-mip.fr">fernando.nino@legos.obs-mip.fr</a> ; <a href="mailto:fabien.leger@legos.obs-mip.fr">fabien.leger@legos.obs-mip.fr</a> ; <a href="mailto:yvan.gouzenes@legos.obs-mip.fr">yvan.gouzenes@legos.obs-mip.fr</a> ;
NOC	F. Calafat	<a href="mailto:Francisco.calafat@noc.ac.uk">Francisco.calafat@noc.ac.uk</a> ;
SkyMAT Ltd	Andrew Shaw	<a href="mailto:agps@skymat.co.uk">agps@skymat.co.uk</a> ;
DGFI-TUM	Marcello Passaro	<a href="mailto:marcello.passaro@tum.de">marcello.passaro@tum.de</a>



## List of Contents

<b>List of Acronyms .....</b>	<b>6</b>
<b>1 Overview .....</b>	<b>8</b>
<b>1.1 References .....</b>	<b>9</b>
<b>2 ATBDs to compute the Sea Level .....</b>	<b>10</b>
<b>2.1 ATBD-1: Orbit altitude .....</b>	<b>11</b>
2.1.1 Selected altimeter standards.....	11
2.1.2 Function .....	11
2.1.3 Algorithm Definition.....	11
2.1.3.1 Input Data .....	11
2.1.3.2 Output Data .....	11
2.1.3.3 Mathematical Statement.....	12
2.1.4 Accuracy .....	13
2.1.5 References .....	13
<b>2.2 ATBD-2: Altimeter range derived from the ALES algorithm .....</b>	<b>14</b>
2.2.1 Selected altimeter standards.....	14
2.2.2 Function- (Preliminary definitions) .....	14
2.2.3 Algorithm Definition.....	16
2.2.3.1 Input Data .....	18
2.2.3.2 Output Data .....	18
2.2.4 Accuracy .....	18
2.2.5 References .....	18
<b>2.3 ATBD-3: Wet troposphere corrections from the GNSS-derived Path Delay (GPD+) algorithm.....</b>	<b>19</b>
2.3.1 Selected altimeter standards.....	19
2.3.2 Function .....	20
2.3.3 Algorithm Definition.....	20
2.3.3.1 Input Data .....	20
2.3.3.2 Output Data .....	23
2.3.3.3 Mathematical statement.....	24
2.3.4 Accuracy .....	26
2.3.5 References .....	28
<b>2.4 ATBD-4: Sea state bias correction derived from the ALES algorithm</b>	<b>28</b>
2.4.1 Selected altimeter standards.....	28
2.4.2 Function .....	28



2.4.3	Algorithm Definition.....	29
2.4.3.1	Input Data .....	29
2.4.3.2	Output Data .....	29
2.4.4	Accuracy .....	29
2.4.5	References .....	30
2.5	ATBD-5: The dual-frequency ionospheric correction filtered by X- TRACK 31	
2.5.1	Selected altimeter standards.....	31
2.5.2	Function .....	31
2.5.3	Algorithm Definition.....	32
2.5.3.1	Input Data .....	32
2.5.3.2	Output Data .....	32
2.5.4	Accuracy .....	32
2.5.5	References .....	34
2.6	ATBD-6: The high frequency fluctuations.....	34
2.6.1	Selected altimeter standards.....	34
2.6.2	Function .....	34
2.6.3	Algorithm Definition.....	35
2.6.3.1	Input Data .....	35
2.6.3.2	Output Data .....	35
2.6.3.3	Mathematical statement.....	35
2.6.4	Accuracy .....	36
2.6.5	References .....	36
2.7	ATBD-7: The dry troposphere derived from ECMWF pressure fields .	37
2.7.1	Selected altimeter standards.....	37
2.7.2	Function .....	37
2.7.3	Algorithm Definition.....	37
2.7.3.1	Input Data .....	37
2.7.3.2	Output Data .....	38
2.7.3.3	Mathematical statement.....	38
2.7.4	Accuracy .....	41
2.7.5	References .....	41
2.8	ATBD-8: The ocean tide height (including long period equilibrium ocean tide) and load tide height .....	41
2.8.1	Selected altimeter standards.....	41
2.8.2	Function .....	41
2.8.3	Algorithm Definition.....	42
2.8.3.1	Input Data .....	42
2.8.3.2	Output Data .....	42





2.8.3.3	Mathematical statement.....	42
2.8.4	Accuracy.....	43
2.8.5	References .....	43
<b>2.9</b>	<b>ATBD-9: Mean Sea Surface Height derived from the X-TRACK</b>	
<b>algorithm</b>	<b>.....</b>	<b>44</b>
2.9.1	Selected altimeter standards.....	44
2.9.2	Function .....	44
2.9.3	Algorithm Definition.....	45
2.9.3.1	Input Data .....	45
2.9.3.2	Output Data.....	45
2.9.4	Accuracy.....	45
2.9.5	References .....	46



## List of Acronyms

ALES	Adaptive Leading Edge Subwaveform
AMR	Advanced Microwave Radiometer
AMSR	Advanced Microwave Scanning Radiometer
ATBD	Algorithm Theoretical Basis Definition
AVISO	French Satellite Altimetry Data Portal of the French Space agency
BH	Brown-Hayne waveform model
CCI	Climate Change Initiative
CNES	French Space Agency: Centre National d'Etudes Spatiales
CorrSSH	Corrected value of Sea Surface Height
DAC	Dynamic Atmospheric Correction
DAD	Dynamic Ancillary Data
DEM	Digital Elevation Model
ERA	ECMWF ReAnalysis
ERS	European Remote Sensing
ESA	European Space Agency
ECMWF	European Centre for Medium-range Weather Forecast
FES	Finite Element System
GDR	Geophysical Data record
GFO	GeoSat Follow-On
GNSS	Global Navigation Satellite System
GPD	GNSS Path Delay
HF	High Frequency
IB	Inverse Barometer
JMR	Jason Microwave Radiometer
JPL	Jet Propulsion Laboratory US
LF	Low Frequency
LRM	Low Resolution Mode
MAD	Medium Absolute Deviation
MSS	Mean Sea Surface
MWR	MicroWave Radiometer
NM	Nelder-Mead
OSTST	Ocean Surface Topography Science Team
POE	Precise Orbit Estimation
RADS	Radar Altimetry Database System
RMS	Root Mean Square
SAD	Static Ancillary Data



SALP	Service d'Altimétrie et de Localisation Précise
SGDR	Sensor Geophysical Data Record
SL_cci	Sea Level Climate Change Initiative project
SLA	Sea Level Anomaly
SLP	Sea Level Pressure
SSB	Sea State Bias
SSH	Sea Surface Height
SSM/I	Satellite Sensor Microwave Imager
SWH	Significant Wave Height
SWT	Surface Water Topography
TG	Tide Gauge
TUM	Technical University of Munich
WTC	Wet Troposphere Correction
ZHD	Zenith Hydrostatic Delay
ZTD	Zenith Total Delay
ZWD	Zenith Wet Delay



## 1 Overview

The objective of this document is to define the Algorithm Theoretical Basis Document (ATBD) for all the algorithms used to compute the altimeter standards along the 20Hz altimeter measurements. Altimeter standards are the components used in the SSH calculation defined by this formula:

$$SLA = Orbit - Range - \sum_{i=0}^N C_i - MSS \quad \text{Eq 1.1}$$

where *Orbit* corresponds to the distance between the satellite and the ellipsoid, *Range* is the distance measured by the altimeter between the satellite and the sea surface, *MSS* is the Mean Sea Surface of the ocean over a long period and  $\sum_{i=0}^N C_i$  is the sum of all the corrections needed to take into account atmospheric effects (wet and dry troposphere, ionosphere, inverse barometer), geophysical phenomena (ocean tides, high frequency atmospheric effects on the ocean) and the sea-surface state (electromagnetic sea-surface bias).

In this project, the best altimeter standards developed in SL\_cci+ project (WP2) were selected in order to calculate the sea-level for climate studies. The selected altimeter standards have been displayed in Table 1.

In this document, we describe the algorithms used to calculate these corrections along the 20Hz altimeter measurements (depending on location: time, latitude, longitude).

Mission	Jason-1,2, Envisat and SARAL	Jason-3
Orbit	POE-E	POE-F
Range	From ALES ( <i>Passaro et al.</i> , 2014)	
Sea State Bias	From ALES ( <i>Passaro et al.</i> , 2015)	
Ionosphere	Dual frequency filtered by X-TRACK ( <i>Birol et al.</i> , 2016)	
Wet troposphere	GPD+ ( <i>Fernandes and Lazaro</i> , 2016)	
Dry troposphere	Model based on ECMWF grids	
Combined atmospheric correction	MOG2D High frequencies forced with analysed ECMWF pressure and wind field [ <i>Carrere and Lyard</i> , 2003] + inverse barometer low frequencies	
Ocean tide	FES 2014 (including ocean tides, long period equilibrium tide, S1 tides...)	
Load tide	FES 2014 ( <i>Carrere et al.</i> , 2012)	
Solid Earth tide	Elastic response to tidal potential [ <i>Cartwright and Tayler</i> , 1971], [ <i>Cartwright and Edden</i> , 1973]	
Pole tide	From Wahr, 1985	
MSS	Computed by X-TRACK by inversion of all the corrected SSH data ( <i>Birol et al.</i> , 2016)	



**Table 1-** New altimeter standards selected for the sea-level calculation in SL\_cci+ project.

## 1.1 References

---

Birol F., N. Fuller, F. Lyard, M. Cancet, F. Niño, C. Delebecque, S. Fleury, F. Toubanc, A. Melet and M. Saraceno, F. Leger, 2016. Coastal applications from nadir altimetry: example of the X-TRACK regional products. *Advances in Space Research*, doi:10.1016/j.asr.2016.11.005.

Cartwright, D. E. and Taylor, R. J., 1971. New computation of the tide-generating potential. *Geophysical Journal of the Royal Astronomical Society*, 23, 45-74.

Cartwright, D. E. and Edden, A. C., 1973. Corrected Tables of Tidal Harmonics. *Geophysical Journal of the Royal Astronomical Society*, 33: 253-264. doi:10.1111/j.1365-246X.1973.tb03420.x.

Carrere L. and Lyard F., "Modeling the barotropic response of the global ocean to atmospheric wind and pressure forcing - comparison with observations", *Geophysical Research Letters*, Vol. 30, NO 6, 1275, doi:10.1029/2002GL016473, 2003

Carrere L., Lyard, F., Cancet, M., Guillot, A., Roblou, L., 2012. FES2012: A new global tidal model taking taking advantage of nearly 20 years of altimetry, Proceedings of meeting "20 Years of Altimetry", Venice 2012.

Fernandes, M., and Clara Lázaro., 2016. GPD+ Wet Tropospheric Corrections for CryoSat-2 and GFO Altimetry Missions. *Remote Sensing* 8 (10): 851. doi:10.3390/rs8100851.

Passaro M., Cipollini P., Vignudelli S., Quartly G., Snaith H., 2014. ALES: A multi-mission subwaveform retracker for coastal and open ocean altimetry. *Remote Sensing of Environment* 145, 173-189, doi: 10.1016/j.rse.2014.02.008.

Passaro M., Fenoglio-Marc L., Cipollini P. 2015. Validation of significant wave height from improved satellite altimetry in the German bight. *IEEE Transactions on Geoscience and Remote Sensing* 53(4): 2146-2156, doi: 10.1109/TGRS.2014.2356331.

Wahr, J. M., 1985. Deformation induced by polar motion. *J. Geophys. Res.*, 90 (B11), 9363- 9368, doi:10.1029/JB090iB11p09363.



## 2 ATBDs to compute the Sea Level

The following table lists the ATBD sections where each algorithm is presented. The number and a short description of the algorithm are listed for each ATBD. The correspondent altimeter standards used in the SSH calculation are also described. Each ATBD is presented in detail in the following chapters.

ATBD Number	Algorithm Description	Altimeter standards	Pages
ATBD-1	Orbit altitude computation	CNES POE-E orbit solutions	Page 11
ATBD-2	Altimeter range computation	ALES algorithm	Page 14
ATBD-3	Wet troposphere correction computation from GNSS-derived Path Delay (GPD+)	Scanning Imager calibrated (GPD+) algorithm	Page 19
ATBD-4	Sea state biases computation	ALES algorithm	Page 28
ATBD-5	Ionosphere correction computation	Dual frequency filtered by X-TRACK	Page 31
ATBD-6	High frequency fluctuations computation	Dynamical atmospheric correction derived from ECMWF model	Page 34
ATBD-7	Dry troposphere derived from ERA-interim pressure fields	Dry troposphere derived from ECMWF pressure fields	Page 37
ATBD-8	Elastic ocean tide height and load tide height computation	FES2014 ocean tide model	Page 41
ATBD-9	Mean sea surface height computation	X-TRACK Mean Sea Surface	Page 44

**Tab. 2** - List of ATBDs corresponding to each algorithm



## 2.1 ATBD-1: Orbit altitude

---

### 2.1.1 Selected altimeter standards

For Jason-1, Jason-2 and SARAL, CNES POE-E orbit solutions have been selected. For Jason-3, the latest solutions are POE-F. They have been provided by CNES in the framework of the SALP project. For more information see Jalabert et al., (OSTST 2015).

### 2.1.2 Function

To compute the orbit altitude (i.e. the altitude of the platform center of gravity above the reference ellipsoid), the orbital altitude rate (i.e. the height rate [m/s] of the satellite at a specific time used to compute the Doppler correction on the altimeter range<sup>1</sup>) with respect to the reference ellipsoid and the location of the measurements from orbit files.

### 2.1.3 Algorithm Definition

#### 2.1.3.1 Input Data

- Datation:
  - 20-Hz altimeter time tag
  - Information to derive the elementary time tags (offset to derive the time-tag of the first elementary measurement, and time interval between two elementary measurements)
- Orbit (DAD):
 

Orbit data covering the time span of the input product, i.e. at regular time steps:

  - Position of the satellite in a terrestrial reference frame:  $\vec{P} = (P_X, P_Y, P_Z)$
  - Velocity of the satellite in a terrestrial reference frame:  $\vec{V} = (V_X, V_Y, V_Z)$
- Processing parameters (SAD):
  - Processing parameters for the orbit interpolation
  - Processing parameters for the determination of the orbit altitude and of the latitude (iterative process): desired accuracy for the orbit altitude, desired accuracy for the latitude
- Universal constants (SAD):
  - Flattening coefficient of the reference ellipsoid
  - Semi major axis of the reference ellipsoid

#### 2.1.3.2 Output Data

- Orbit altitudes
- Orbital altitude rates
- Location, i.e. latitude and longitudes

---

1 taken from <https://sentinel.esa.int/web/sentinel/sentinel-3-altimetry-wiki/-/wiki/Sentinel+Three+Altimetry/Orbital+Altitude+Rate;jsessionid=437F472CC6B9704674092D3809BD>



### 2.1.3.3 Mathematical Statement

- The orbit altitude  $h$ , the latitude  $\varphi$  and the longitude  $\lambda$  corresponding to an input 20-Hz or 1-Hz altimeter time-tag  $t$ , are computed as follows:
  - $N$  (typically  $N=8$ ) position vectors are selected from the input orbit file ( $N/2$  before and  $N/2$  after the altimeter time tag), and are interpolated at the altimeter time tag using Everett's formula (Abramowitz, 1965).
  - The interpolated position  $\vec{P}_S = (P_{SX}, P_{SY}, P_{SZ})$  of the satellite is then projected onto the reference ellipsoid to provide  $h$ ,  $\varphi$  and  $\lambda$  (see Nouel, 1980 or Klinkrad, 1985 or Guinn, 1990).
- The orbital altitude rate with respect to the reference ellipsoid ( $h'$ ) corresponding to an input 20-Hz or 1-Hz altimeter time-tag  $t$  is computed as follows, using the corresponding latitude  $\varphi$  and longitude  $\lambda$  (computed as defined above):
  - The position  $\vec{P}_N = (P_{NX}, P_{NY}, P_{NZ})$  of the geodetic subsatellite point (denoted as the nadir point) is derived from  $\varphi$  and  $\lambda$ , using a simple change of co-ordinate system (see Nouel, 1980).
  - The normalized line of sight vector, in the direction NS defined by the satellite (S) and the corresponding nadir point (N) is then computed by:

$$\vec{L} = \frac{\vec{P}_S - \vec{P}_N}{\|\vec{P}_S - \vec{P}_N\|} \quad \text{Eq 2.1}$$

- $M$  (typically  $M=8$ ) velocity vectors are selected from the input orbit file ( $M/2$  before and  $M/2$  after the altimeter time tag), and are interpolated at the altimeter time tag using Everett's formula (Abramowitz, 1965).
- The orbital altitude rate  $h'$  is finally obtained by forming a scalar product of the interpolated satellite velocity vector  $\vec{V}_S = (V_{SX}, V_{SY}, V_{SZ})$  with the normalized line of sight vector  $\vec{L}$  (Dumont et al., 1997), i.e. by:

$$h' = \frac{V_{SX} \cdot (P_{SX} - P_{NX}) + V_{SY} \cdot (P_{SY} - P_{NY}) + V_{SZ} \cdot (P_{SZ} - P_{NZ})}{\sqrt{(P_{SX} - P_{NX})^2 + (P_{SY} - P_{NY})^2 + (P_{SZ} - P_{NZ})^2}} \text{ m/s} \quad \begin{matrix} 2.1.3.3.1.1.1.1 \text{ Eq} \\ 2. \\ 2 \end{matrix}$$

- The points and vectors used in the above descriptions are illustrated in **Figure 1.1**



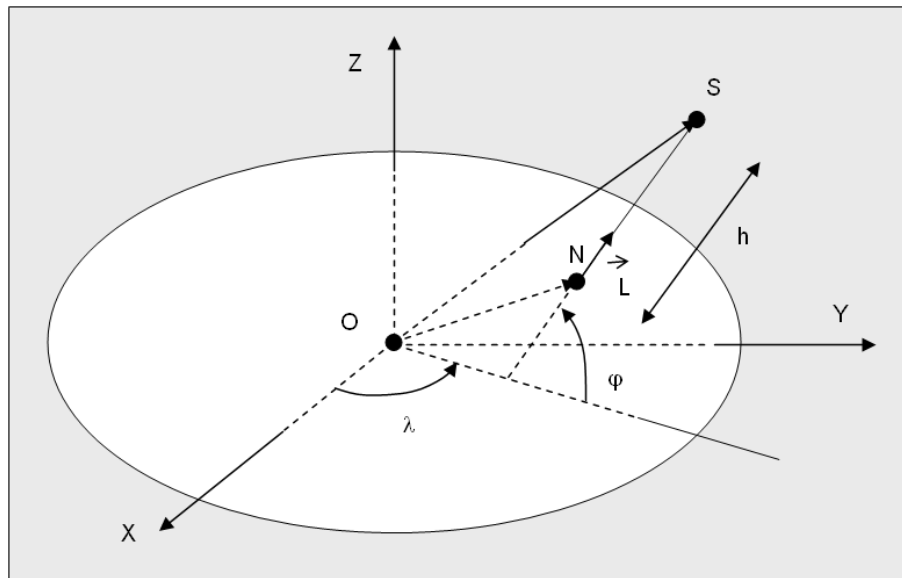


Figure 1.1 - Computation of the orbit altitude and the orbital altitude rate with respect to the reference ellipsoid

### 2.1.4 Accuracy

The error due to Everett interpolation method is smaller than 1 mm if the number  $N$  of orbit points taken into account is large enough (typically  $N=8$ , i.e. 4 points before and 4 points after the altimeter time) (Dumont et al., 1997).

### 2.1.5 References

- Abramowitz M. And Stegun I.A., Handbook of Mathematical Functions, Dover Publication Inc. N.Y., 1965
- Dumont J.-P., J. Stum and O. Z. Zanife, 1997. Algorithms Definition and Accuracy, RA2/MWR LOP, CLS.OC/NT/96.038, Issue 2rev1, 14 November 1997, Nomenclature : PO-NT-RAA-0004-CLS, [http://envisat.esa.int/support-docs/pdf/ra2mwr\\_ada.pdf](http://envisat.esa.int/support-docs/pdf/ra2mwr_ada.pdf)
- Guinn, J.R., Definition of Reference Earth Ellipsoid for TOPEX/POSEIDON, JPL Interoffice Memorandum, 314.5-1409, 15 February 1990.
- Jalabert E. et al., "JASON-2, SARAL AND CRYOSAT-2 STATUS", Precise Orbit Determination Splinter, [https://meetings.aviso.altimetry.fr/fileadmin/user\\_upload/tx\\_ausylsseminar/files/OSTS\\_T2015/POD-01-Jalabert.pdf](https://meetings.aviso.altimetry.fr/fileadmin/user_upload/tx_ausylsseminar/files/OSTS_T2015/POD-01-Jalabert.pdf)
- Klinkrad, H., ERS-1, Algorithms for orbit prediction and for the determination of related static and dynamic altitude and groundtrace quantities, ESA, ER-RP-ESA-SY-0001, 1985.
- Nouel, F., Les Repères de l'Espace et du Temps, Le Mouvement du Véhicule Spatial en orbite, Cours de Technologie Spatiale, CNES, 1980.



## 2.2 ATBD-2: Altimeter range derived from the ALES algorithm

---

### 2.2.1 Selected altimeter standards

The retracking of the LRM missions included in this project (Jason-1, Jason-2, Jason-3, Envisat, SARAL) is based on the ALES retracking algorithm. The ALES retracking algorithm is a Python routine coded in-house at TUM and based on the algorithm described in Passaro et al., 2014. Changes and adaptations of this algorithm for the different missions are reported below.

As according to the project proposal, the retracking of the Delay-Doppler missions included in this project (Sentinel-3a&b) is an experimental empirical retracker based on ALES and adapted to the Sentinel-3a,b dataset. At the same time, the official output, based on the SAMOSA2-retracker, is provided to the Consortium, which will decide whether to prefer the experimental retracker or the standard one. The experimental retracker for Delay-Doppler missions will be described in the next issue of this document.

### 2.2.2 Function- (Preliminary definitions)

#### BROWN-HAYNE MODEL

ALES is based on the Brown-Hayne (BH) functional form that models the radar returns from the ocean to the satellite. The BH theoretical ocean model [Brown (1977), Hayne (1980)] is the standard model for open ocean retrackers and describes the average return power of a rough scattering surface (i.e. what we simply call waveform). The return power is modelled as follows (equations as reported in Passaro et al., 2014):

$$V_m = a_\xi P_u \frac{[1 + \text{erf}(u)]}{2} \exp(-v) + T_n$$

where:

$$a_\xi = \exp\left(\frac{-4 \sin^2 \xi}{\gamma}\right); \quad \gamma = \sin^2(\theta_0) \frac{1}{2 \ln(2)}$$

$$u = \frac{t - \tau - c_\xi \sigma_c^2}{\sqrt{2} \sigma_c}; \quad v = c_\xi (t - \tau - 0.5 c_\xi \sigma_c^2);$$

$$\sigma_c^2 = \sigma_p^2 + \sigma_s^2;$$

$$\sigma_s = \frac{SWH}{2c}$$

$$c_\xi = b_\xi a;$$

$$a = 4c / \left[ \gamma h \left( 1 + \frac{h}{R_e} \right) \right]$$

$$b_\xi = \cos(2\xi) - \frac{\sin^2(2\xi)}{\gamma}$$

where erf(u) denotes the error function, c is the speed of light, h the satellite altitude, R<sub>e</sub> the Earth radius, ξ the off-nadir mispointing angle, θ<sub>0</sub> the antenna beam width, τ the Epoch with respect to the nominal tracking reference point, σ<sub>c</sub> the rise time of the leading edge (depending on a term σ<sub>z</sub> linked to SWH and on the width of the radar point target response σ<sub>p</sub>), P<sub>u</sub> the amplitude of the signal and T<sub>n</sub> the thermal noise level.

---

#### NELDER MEAD ALGORITHM

The Nelder-Mead (NM) algorithm is a simplex optimisation method that does not use the derivatives of its cost function, whilst it searches for the minimum in a many-dimensional space (Nelder and Mead, 1965). Specifically, considering m parameters to be estimated, given that a simplex of



dimension  $m$  is a polytope of the same dimension and with  $m + 1$  vertices characterised by  $m + 1$  cost function values, NM generates at each step a new point whose cost function is compared with its value at the vertices. If it is smaller, the point becomes a vertex of the new simplex and a new iteration is generated (Nelder and Mead, 1965). Convergence is reached when the diameter of the simplex is smaller than a specified tolerance.

In ALES, the objective function to be minimised is:

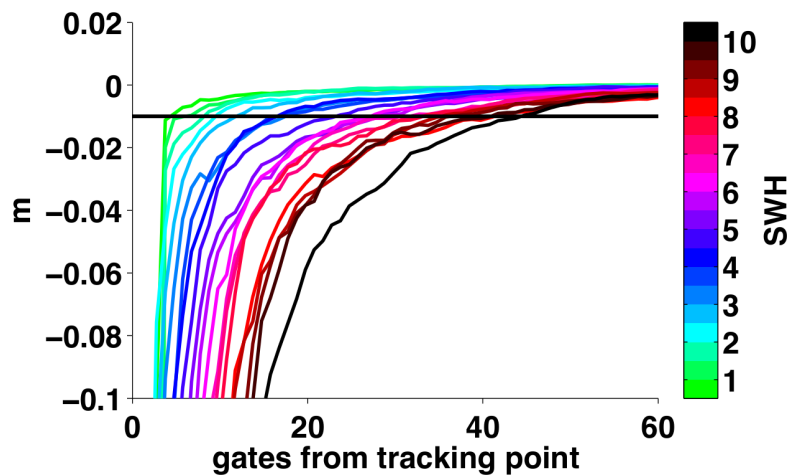
$$C = \sum (W * R^2) ,$$

where  $W$  is the vector of weights and the residual  $R$  is the difference between the real and the fitted waveform. NM is applied using the Python package `scipy.optimize.minimize`.

## ALES COEFFICIENTS

The key concept of the ALES subwaveform is that a leading-edge only retracker, although also providing results waveforms that do not conform to the BH model, has worse noise performances than a full-waveform retracker and therefore would not guarantee the homogeneity of the result. For best accuracy the subwaveform width for the second pass must be optimised such that it fully includes all gates comprising the leading edge, but with minimal contribution from the trailing edge, where artefacts such as bright target responses may prevent the BH model from accurately describing the shape. Defining startgate and stopgate the first and last gate of the subwaveform of choice, in effect the issue is one of defining an appropriate stopgate for a given SWH. The relationship between SWH and stopgate was derived from Montecarlo simulations. For each value of SWH ranging from 0.5 to 10 m in steps of 0.5 m, 10000 echoes were simulated with the BH model adding realistic Rayleigh noise, and then averaged to create a simulated high-rate waveform. The resulting waveforms were retracked over the entire waveform, and then over sub-waveform windows with startgate=1 and variable stopgate, and the RMS errors (RMSE) were computed.

The difference of the RMSEs between the "full waveform" estimate and the subwaveform estimates is displayed as a function of the stopgate position in the figure below (upper panel). The x axis is, in practice, the width of the sub-waveform, expressed as number of gates from the tracking point to the stopgate. The results for each SWH level are coded in different colours. The curves converge asymptotically to the full waveform estimates, as expected for this idealised case of "pure-Brown" response of the ocean surface. The relation needed in ALES is shown in the panel below and is obtained by setting a tolerance in the RMSE difference of the SWH. In order for ALES to optimise the need to retrieve signals whose trailing edge is corrupted, the tolerance bar was set to 1 cm at 20 Hz, i.e. 0.22 cm at 1 Hz.



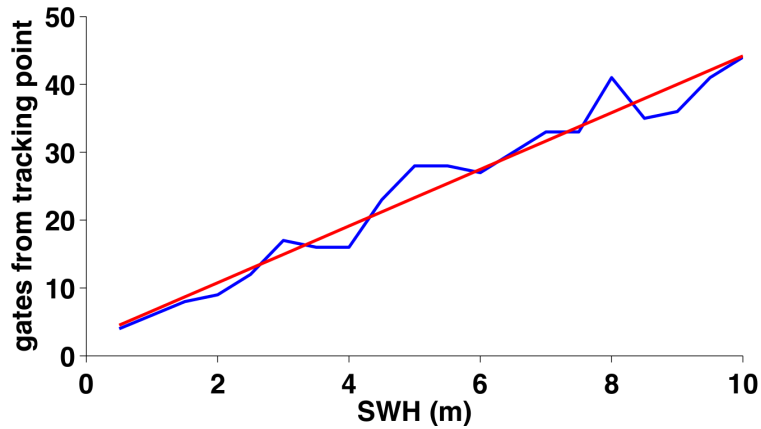
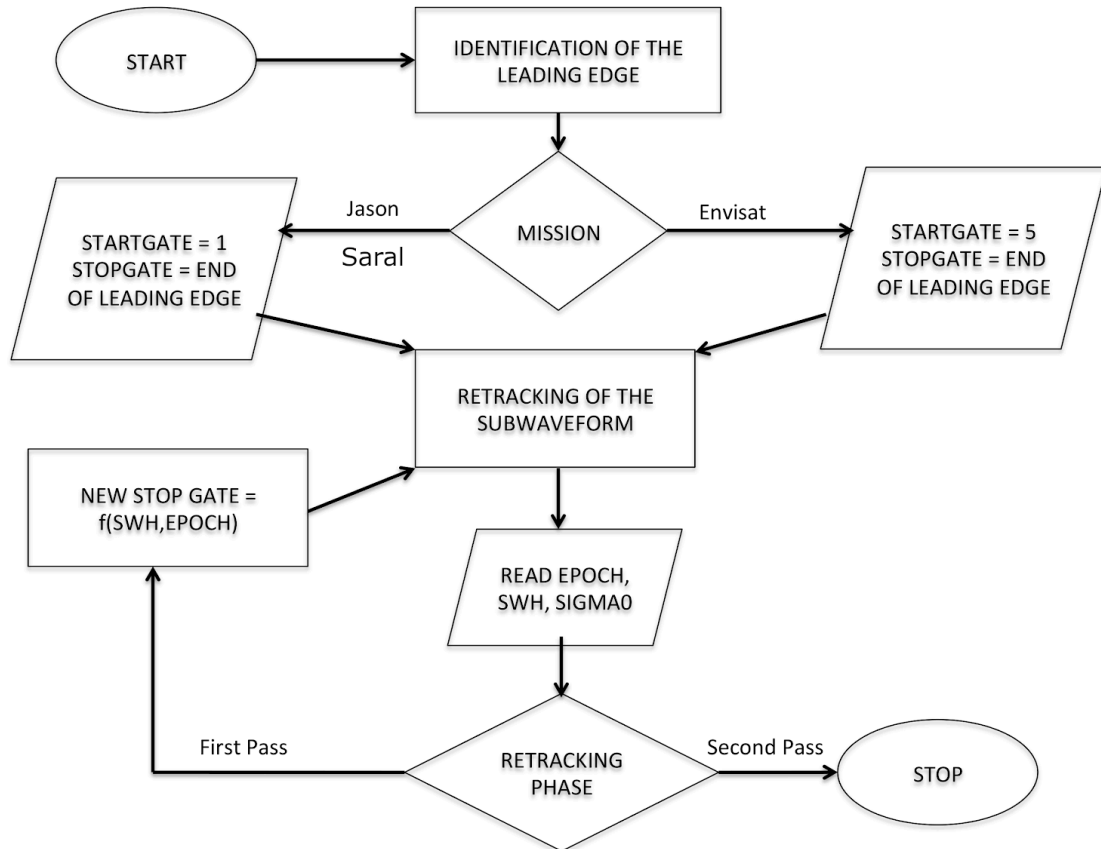


Figure 2.1: (Up) Difference of the RMSEs in the Range computation between the "full waveform" estimate and the subwaveform estimates as a function of the stopgate position. (Below): linear relationship obtained by setting a tolerance in the RMSE difference of the Range in the upper plot. In order for ALES to optimise the need to retrieve signals whose trailing edge is corrupted, the tolerance bar was set to 1 cm at 20 Hz.

### 2.2.3 Algorithm Definition

ALES is a two-pass retracker. The retracking of each waveform follows the procedure described in the following flow diagram:





The functional form used to fit the real waveforms is the Brown-Hayne model as described in the following section. The original waveforms of any altimeter mission are discretized in elements called “gates”. In ALES, the first gate number is identified as 0 and the x-axis of a waveform is sampled in time. For example for Jason-3:

$$x=[0,1*\tau,2*\tau,\dots,103*\tau]$$

Where  $\tau$  is the spacing between two consecutive gates in time (3.125 ns in Jason-3).

The Leading Edge identification includes also the normalisation of the waveform and is performed following these substeps:

- 1) The waveform is normalised with normalisation factor N, where  $N = 1.3 * \text{median}(\text{waveform})$
- 2) The leading edge starts when the normalised waveform has a rise of 0.01 units compared to the previous gate (startgate)
- 3) At this point, the leading edge is considered valid if, for at least four gates after startgate, it does not decrease below 0.1 units (10% of the normalised power).
- 4) The end of the leading edge (stopgate) is fixed at the first gate in which the derivative changes sign (i.e. the signal start decreasing and the trailing edge begins), if the change of sign is kept for the following 3 gates.

The scope of the normalisation is indeed to take as reference power a value close to the maximum of the leading edge and, in the case of oceanic waveforms with standard trailing edge noise, the proposed factor N is a good approximation.

The first pass of ALES involves a subwaveform that goes from startgate to stopgate+1. It is therefore a leading-edge-only subwaveform retracking. The vector of weights is filled with 1s. The convergence is therefore found by means of an unweighted Nelder-Mead estimator (see previous section of preliminary definitions). The unknowns and the corresponding initial conditions applied are:

$$\tau = \text{startgate} - 1; \sigma_c = (\text{stopgate} - \text{startgate}) / (2 * \sqrt{2}); P_u = 2 * \text{mean}(D[\text{startgate} : \text{stopgate}])$$

Where D is the normalised waveform. In case convergence is not reached, a new attempt is performed extending the subwaveform by two gates, until convergence or until the waveform limit.

After the first pass, the ALES coefficients are applied to extend the subwaveform. The issue is one of defining an appropriate new stopgate for the second pass retracking based upon the SWH estimates from the first pass. The Stopgate is found using the following:

$$\text{Stopgate} = \text{Ceiling}(\text{Tracking point} + \text{ALEScoeff0} + \text{ALEScoeff1} * \text{SWH})$$

where:

Envisat:

$$\begin{aligned} \text{ALEScoeff0} &= 2.43; \\ \text{ALEScoeff1} &= 4.18; \end{aligned}$$

Saral:

$$\begin{aligned} \text{ALEScoeff0} &= 2.90; \\ \text{ALEScoeff1} &= 3.37; \end{aligned}$$

Jason-1, Jason-2, Jason-3:

$$\begin{aligned} \text{ALEScoeff0} &= 1.37 \\ \text{ALEScoeff1} &= 4.51 \end{aligned}$$

Using the new limits of the subwaveform, a second NM estimation is performed using the same initial conditions of the first pass.



The “Fitting Error on the leading edge” (Err) is used as a quality measure for the fitting. It is computed as the RMS difference between the fitted and the real waveform, considering only the gates of the leading edge.

### 2.2.3.1 Input Data

- Sensor Geophysical Data Records

### 2.2.3.2 Output Data

- Range
- SWH
- $\sigma_0$
- Fitting Error on the Leading Edge

### 2.2.4 Accuracy

The assessment of the accuracy of the Range based on ALES is part of the tasks of the Validation of this project and therefore does not belong to this document. Here we report the synthesis of the main results based on previous studies:

- ALES is able to provide more reliable 20-Hz data for the tested missions in areas where even 1-Hz averages are flagged as unreliable in standard products. Application of the ALES retracker led to roughly a half of the analysed tracks showing a marked improvement in correlation with the tide gauge records, with the rms difference being reduced by a factor of 1.5 for Jason-1 and Jason-2 and over 4 for Envisat in the Adriatic Sea (at the closest point to the tide gauge). [Passaro et al., 2014]
- RMS Differences between the sinusoids corresponding to the annual cycle of the sea level estimated by the tide gauges and the sinusoids estimated from different altimetry data sets in the North Sea - Baltic Sea transition zone (including global gridded and along-track SL\_cci product and RADS database) showed that only ALES-based data were in accordance with the Tide Gauge within 1.5 cm. [Passaro et al., 2015]

### 2.2.5 References

- Brown, G. S., 1977. The average impulse response of a rough surface and its applications. IEEE Journal of oceanic engineering, 2 (1), 67-74, DOI: 10.1109/JOE.1977.1145328.
- Hayne, G., 1980. Radar altimeter mean return waveforms from near-normal-incidence ocean surface scattering. IEEE Transactions on Antennas and Propagation, 28(5), pp.687-692.
- Nelder, J.A. and Mead, R., 1965. A simplex method for function minimization. The computer journal, 7(4), pp.308-313.
- Passaro M., Cipollini P., Vignudelli S., Quartly G., Snaith H., 2014. ALES: A multi-mission subwaveform retracker for coastal and open ocean altimetry. Remote Sensing of Environment 145, 173-189, doi: 10.1016/j.rse.2014.02.
- Passaro M., Fenoglio-Marc L., Cipollini P. 2015. Validation of significant wave height from improved satellite altimetry in the German bight. IEEE Transactions on Geoscience and Remote Sensing 53(4): 2146-2156, doi: 10.1109/TGRS.2014.



## 2.3 ATBD-3: Wet troposphere corrections from the GNSS-derived Path Delay (GPD+) algorithm

### 2.3.1 Selected altimeter standards

The wet tropospheric path delay is almost proportional to the integrated water vapour content of the atmosphere and strongly affects the range measured by the altimeter (up to 50 cm). Meteorological models do not properly describe the high water vapour variability in space and time, therefore a dedicated microwave radiometer is added to the mission. The GPD+ algorithm has been selected for the estimation of the wet tropospheric correction for climate applications, for all missions with an onboard MWR.

Name	Description	Mission applicability
GNSS-derived Path Delay Plus (GPD+) algorithm	<p>Main features of the GPD+ algorithm:</p> <ul style="list-style-type: none"> <li>The GPD+ are wet path delays based on: i) WTC from the on-board microwave radiometer (MWR) measurements whenever they exist and are valid; ii) new WTC values estimated by data combination, through space-time objective analysis (OA) of all available data sources, whenever the previous are considered invalid.</li> <li>In the estimation of the new WTC values, the following data sets are used: valid measurements from the on-board MWR, from water vapour products derived from a set of near 20 scanning imaging radiometers (SI-MWR) on board various remote sensing satellites and wet path delays derived from GNSS (Global Navigation satellite Systems) coastal and island stations.</li> <li>In the estimation process, WTCs derived from an atmospheric model, such as the European Centre for Medium-range Weather Forecasts (ECMWF) ReAnalysis (ERA) Interim or the operational (Op) model, are used as first guess and adopted in the absence of measurements.</li> <li>At each altimeter point with an invalid MWR value, the wet tropospheric correction is estimated, along with the associated mapping error, using a linear space-time objective analysis technique that takes into account the spatial and temporal variability of the wet path delay field and the accuracy of each data set used.</li> <li>All radiometer data sets have been inter-calibrated, using the set of Sensor Microwave Imager (SSM/I) and SSMI/I Sounder (SSM/IS) on board the Defense Meteorological Satellite Program (DMSP) satellite series (FXX) as reference.</li> </ul>	Jason-1, Jason-2, Jason-3, Envisat, SARAL



## 2.3.2 Function

The initial aim of this algorithm was to provide the wet tropospheric correction in the coastal zone, where the MWR measurements become invalid due to land contamination in the radiometer footprint (~25 km). In the present implementation the WTC is provided globally for all altimeter ocean measurements.

Whenever an MWR measurement is considered valid, the correction equals the MWR-based wet path delay. For every ocean point along the altimeter ground track for which the MWR-based WTC has been considered invalid according to a set of criteria, a new estimate is obtained along with its associated error. These include not only coastal points, but also open ocean, including high latitudes. Therefore, apart from land contamination, rain and ice contamination are also spotted and corrected.

The algorithm ensures the continuity and consistency of the correction in the open-ocean / coastal transition zone and also at high latitudes.

Moreover, the calibration with respect to the SSM/I and SSM/IS set of sensors ensures the temporal consistency between missions, due to the well-known stability and independent calibration of these sensors.

## 2.3.3 Algorithm Definition

### 2.3.3.1 Input Data

- 1) Wet path delays from valid MWR measurements at the nearby locations around the point of estimation. Due to the time difference between adjacent satellite tracks, in practice only points from a single track are used, the track to which the point of estimation belongs. The baseline MWR data used for the different missions are:
  - Jason-1 - MWR values present in the AVISO CORSSH products (JMR Replacement product changed by the Composite algorithm in the band 0-50 km around the coast). For use in the GPD+ estimations, on top of the usual analysis for identification of invalid MWR values, all points in the band 0-50 km from coast were flagged as invalid and estimated. The reason for adopting this Jason-1 MWR product is to remove the “anomaly” detected in the JMR Enhanced product used in the previous GPD WTC versions;
  - Jason-2&3 - AMR GDR-D product, already enhanced near the coast, Brown (2010);
  - Envisat and SARAL - The MWR measures the brightness temperatures in the nadir path at 23.8 GHz and 36.5 GHz. Brightness temperatures measurements are combined with the estimation of the Ku-band backscatter coefficient to obtain the path delay in the satellite range measurement due to the water vapor content. A neural network is used to obtain the WTC. Three models are also given in the GDR: (1) ECMWF analysis, (2) values computed from the integration of ECMWF ERA-Interim profiles at the altitude of the measurement and a model for S1 and S2 atmospheric tides, and (3) GPD+.
- 2) Zenith wet delays (ZWD) derived at a network of coastal GNSS stations. GNSS data from about 800 stations were used (Figure 3.1). These include zenith total delays (ZTD) computed at UPorto and ZTDs available online at a set of stations from IGS (International GNSS Service), EPN (EUREF Permanent Network), SuomiNet and from the German Bight provided by the Technische Universität Darmstadt in the scope of this project. Only stations up to 100 km from the coast and with an orthometric height < 1000 m were considered. The first condition aims at selecting only coastal stations; the second is due to the fact that the expression for the height dependence of the WTC by Kouba (2008), used to reduce the ZWD from Station height to sea level, is valid only up to 1000m.

The quantity estimated at each GNSS station is the total tropospheric correction (ZTD) at





station level given by the sum of the zenith hydrostatic delay (ZHD) and zenith wet delay (ZWD) through appropriate mapping functions related to the angle of elevation. The quantity used in coastal altimetry is the ZWD at sea level. The latter is obtained from the ZTD at station level by computing the dry correction or zenith hydrostatic delay (ZHD) from the ERA Interim SLP (Sea Level Pressure) field using the Saastamoinen model (Davis et al., 1985) and reducing ZHD and ZWD fields to sea level using the procedure by Kouba (2008), with the modifications introduced by Fernandes et al. (2015).

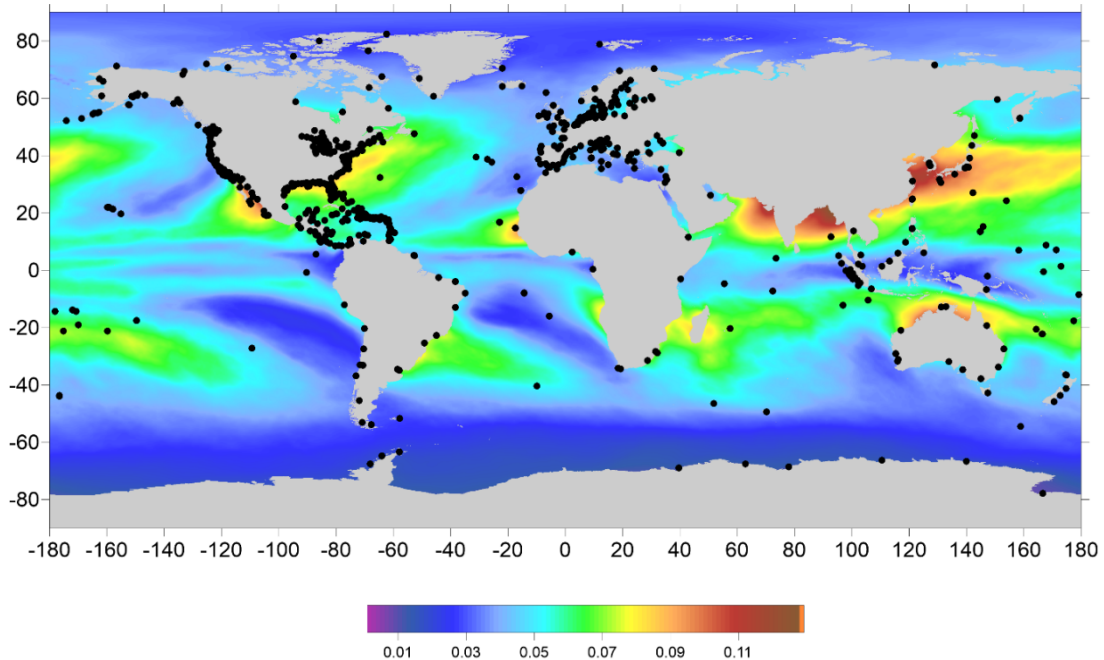


**Figure 3.1** - Location of GNSS stations used in the GPD+ estimations. The background picture is the map of the standard error of the wet tropospheric correction, in metres, computed from two years of ECMWF model fields

- 3) Water vapour products from a set of 17 scanning imaging radiometers on board various remote sensing satellites available from two main sources: NOAA CLASS System (AMSU on NOAA-15, 16, 17, 18, 19, MetOp-A and MetOp-B) and Remote Sensing Systems (AMSR-E on Aqua, AMSR-2 on GCOM-W, WindSat on Coriolis, TMI on TRMM, SSM/I on DMSP satellites F10, F11, F13, F14, SSM/IS on F16, F17), see figure 3.2.

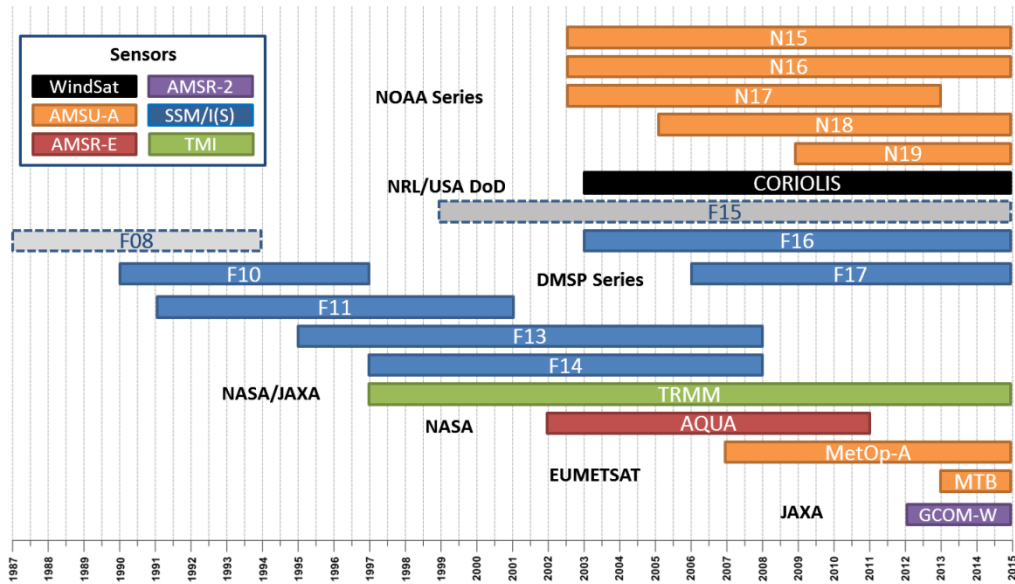


Figure 3.2 - Set of Si-MWR sensors used in the GPD+ estimations (F08 and F15 were not used due to their instable behavior (Wentz, 2013)).

- 4) Tropospheric delays from the European Centre for Medium-range Weather Forecasts (ECMWF) operational model (used for the most recent missions: Jason-2, CryoSat-2 and SARAL) and from the ERA Interim, used for the remaining missions.

ECMWF provides global  $0.125^\circ \times 0.125^\circ$  (Operational model) or  $0.75^\circ \times 0.75^\circ$  (ERA Interim) grids of several atmospheric parameters every 6 hours (Miller et al., 2010, Dee et al., 2011). In the scope of this study, the atmospheric fields of three single-level parameters of the two aforementioned models were used for the period [1991 - 2015] and for the whole globe:

- Sea level pressure (SLP)
- Surface temperature (2-meter temperature, 2T)
- Integrated water vapour (Total Column Water Vapour, TCWV)

These parameters are used both in the ZWD processing described above and to compute a model-derived WTC for each altimeter along-track position by space-time interpolation from the two closest grids, 6-hours apart. These model-derived WTC are used as first guess in the OA estimation and as adopted GPD+ values in the absence of observations.

### Sensor calibration

To ensure consistency and the long term stability of the WTC, the large set of radiometers used in the GPD+ estimations have been inter-calibrated, using the set of SSM/I and SSM/IS on board the DMSP satellite series (F10, F11, F13, F14, F16 and F17) as reference, due to their well-known stability and independent calibration (Wentz, 2013). The calibration was performed in three steps:

- Step1 - TP, J1, J2 were calibrated against the FXX series
- Step2 - All 35-day missions were calibrated against TP, J1, J2
- Step3 - remaining SI-MWR were calibrated against TP, J1, J2

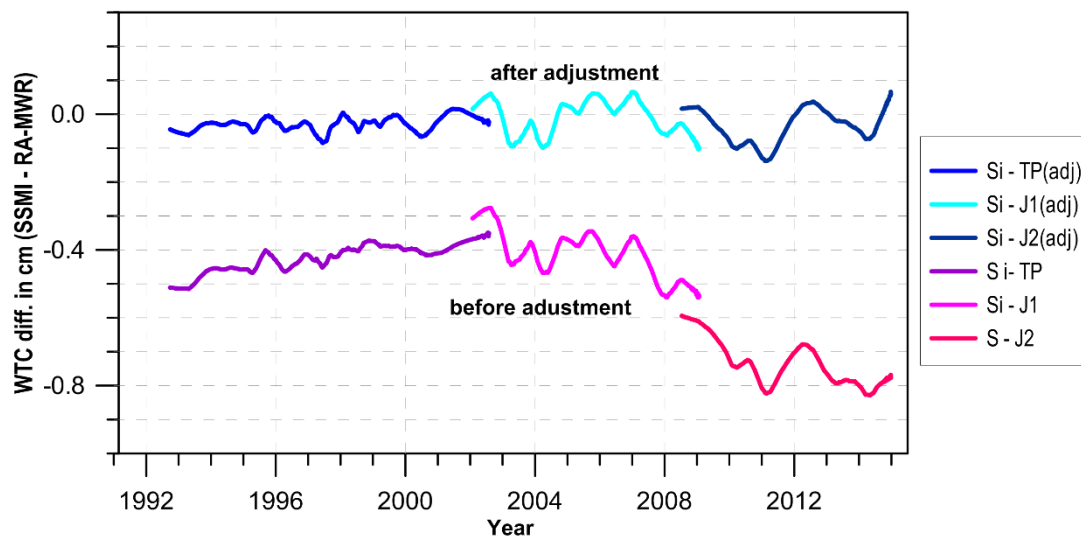
The adjustment model uses three parameters: Offset ( $a$ ), scale factor ( $b$ ) and trend ( $c$ ), where  $X$  is the observation,  $Y$  is the adjusted value and  $T$  is the date of observation:

$$Y = a + bX + c(T - T_0), \quad T_0 = 1992 \quad \bullet \quad \text{Eq 3.3}$$

In step 1 match points between SSM/I and SSM/IS sensors and MWR on board reference altimetric mission (TP, J1, J2) were calculated. Only points with time difference  $\Delta T < 45$  min and distance



$\Delta D < 50$  km were considered (Fernandes et al., 2013). The WTC data from each reference altimetric mission were then adjusted to the WTC data from SSM/I and SMM/IS set of sensors (Figure 3.3).



• **Figure 3.3** - Differences in WTC (cm) from SSM/I, SSM/IS and MWR on board satellite altimetry reference missions, before and after calibration.

In step 2 the WTC from each 35-day mission (E1, E2, EN, SA) were calibrated against the WTC from the reference missions (TP, J1, J2) by minimizing the crossover differences between each sun-synchronous 35-day mission and the altimetry reference missions. Only crossover points with a  $\Delta T < 180$  min were considered. This value was found to be the best compromise between the number of crossovers and the minimum time interval.

In step 3 the WTC from all remaining SI-MWR (except the FXX series) sensors were adjusted to the WTC from the altimetric reference missions.

For the reference altimetric missions the offsets are in the range -0.8 to 0.6 cm, the scale factors in the range 0.96 to 0.99 and the trends in the range -0.22 to 0.15 mm/yr. For the 35-day altimetric missions the offsets are in the range -1.3 to 0.8 cm, the scale factors in the range 0.96 to 0.99 and the trends in the range 0.07 to 0.17 mm/yr. For the remaining SI-MWR the offsets are in the range -1.1 to 0.0 cm, the scale factors in the range 0.99 to 1.02 and the trends in the range -0.26 to 0.25 mm/yr. Although these parameters are generally small, they have an effect in the global sea level variation mainly at decadal time scales and in the regional mean sea level.

### 2.3.3.2 Output Data

For each ocean and coastal measurement point along the satellite track, the output fields listed below are provided. In addition to ocean points, to help on interpolation to higher data rates, the first land point of each track is also selected, provided it is within 50 km from the coastline (brown points in Figure 3.5).

- wet\_GPD** - wet tropospheric correction (metres)
- GPD\_error** - formal error of the wet\_GPD estimate (metres)
- GPD\_flag** - validity flag of the wet\_GPD estimate:
  - 0 - non-corrupted ocean points. For these wet\_GPD = rad\_wet\_tropo\_cor.
  - 1 - wet\_GPD is a valid estimate.



- 2 - there were no observations to perform the GPD estimation. For these points wet\_GPD is set to the model-derived WTC.
- 3 - Unreliable GPD estimate, according to algorithm internal criteria.

In practice, the wet\_GPD wet tropospheric correction is valid when GPD\_flag = 0, 1 or 2. For points with GPD\_flag = 0 the correction is the original radiometer correction, possibly scaled due to sensor calibration (see text about sensor calibration above); for points with GPD\_flag = 1 a valid estimate of the wet tropospheric correction has been obtained from the available observations; when GPD\_flag = 2 the correction is the adopted model used as first guess in the estimation process.

### 2.3.3.3 Mathematical statement

The GNSS-derived Path Delay (GPD) methodology, developed at UPorto, started as a coastal algorithm in the scope of the ESA project COASTALT (Development of radar altimetry data processing in the oceanic coastal zone), aiming at removing the land effects in the microwave radiometers on board the altimeter missions (Fernandes et al., 2010). Then the methodology evolved to cover the open ocean, including high latitudes, correcting for invalid observations due to land, ice and rain contamination and instrument malfunction (Fernandes et al., 2015). After adequate algorithm tuning, it is applicable to any other altimetric mission with or without an on-board MWR.

The most recent version of this algorithm, designated GPD Plus (GPD+), developed in phase II of the SL\_cci project, includes the previously designated GPD and DComb (Data Combination) algorithms, the latter developed for CryoSat-2 in the scope of the CP40 (CryoSat Plus for Oceans) project.

The core of the GPD algorithm is based on a linear space-time objective analysis (OA) technique (Bretherton et al., 1976). The statistical technique interpolates the wet path delay values at each altimeter ground-track point with invalid MWR measurements from the nearby (in space and time) observations. It updates a first guess value known a priori at each location and epoch and provides a quantification of the mapping error associated with each estimate.

Thus, the GPD+ are wet path delays based on: i) WTC from the on-board MWR measurements whenever they exist and are valid; ii) new WTC values estimated by data combination of all available observation in the vicinity of the estimation point, whenever the previous are considered invalid.

The spatial and temporal variability of the ZWD field is taken into account by the correlation function which, in the absence of the knowledge of an empirical covariance model of the background field, can take the form of a product of two stationary Gaussian decays (Leeuwenburgh, 2000; Schüler, 2001).

The space correlation scales were determined from a set of ECMWF operational model grids at  $0.125^\circ \times 0.125^\circ$ , well distributed over the year 2013. The computations were performed for a grid of points centered on  $2^\circ \times 2^\circ$  "boxes". For each of these central points, analyses were made on boxes of  $2^\circ \times \Delta\lambda^\circ$ , where  $\Delta\lambda = \min(2^\circ / \cos \varphi, 2^\circ)$ , where  $\varphi$  and  $\lambda$  stand for latitude and longitude, respectively. This warrants that all analyses are made on boxes of approximately the same size. For each box, the correlation between all pairs of points separated by a distance R, for classes of R spaced by 10 km, were determined. The set (R, corr(R)) forms the correlation table for each box. The corresponding correlation scale D is obtained by either fitting a Gaussian function to the correlation table or by computing the value of R corresponding to a correlation equal to  $1/e$ . Both approaches give similar results and the resulting spatial correlation scales are within 40 to 93 km (Figure 3.4).

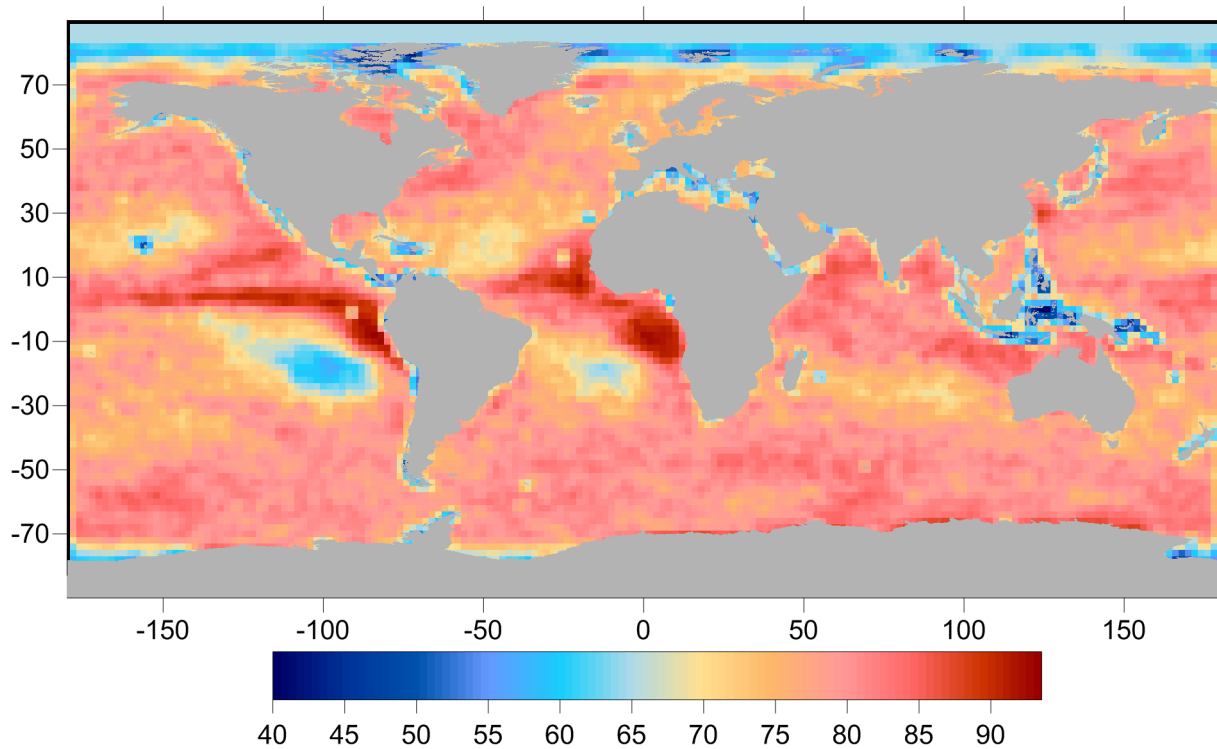


**Figure 3.4** - Spatial correlation scales (in km) for the WTC as determined from a set of ECMWF Operational Model grids at  $0.125^\circ \times 0.125^\circ$  well distributed over the year 2013.

For the temporal correlation scales, in the absence of time to perform a similar analysis within the time frame of this project, the value of 100 minutes quoted by Bosser et al. (2007) was adopted.

The data used for each WTC estimation are the WTC observations from all data sets within the spatial and temporal influence regions, centred at the location and instant of the altimeter measurement at which the estimation is required; those ranges should equal the spatial and temporal correlation scales. However, since the period of most SI-MWR missions is in the range 100-105 minutes, the temporal influence region has been enlarged to 110 minutes for the SI-MWR dataset.

To balance the weight between the various types of observations, values of 0.5 cm have been adopted for the white noise of both MWR and GNSS-derived ZWD (Fernandes et al., 2015), whereas the associated error for each SI-MWR sensor was computed based on the standard deviation of the differences between each sensor and the values of the MWR on board the reference altimetric missions at matching points. These values are in the range 0.8 cm (for Windsat, AMSR-E and AMSR-2) and 1.2 cm (for NOAA-15, NOAA-17 and MetOp-B).

The GPD algorithm was designed to compute the WTC at ocean measurements. Initially, the computation was restricted to coastal areas, where a set of GNSS inland stations can be found. In the present implementation an estimate is obtained for every ocean point along the altimeter ground track for which the WTC computed from MWR measurements has been considered invalid. The validity of an MWR measurement is set by an MWR rejection flag (flag\_MWR\_rej) according to the following criteria

- flag\_MWR\_rej = 1 - if the rad\_surf\_type flag is 1 (land contamination)
- flag\_MWR\_rej = 2 - if the point distance from coast is less than 30 Km (land contamination).
- flag\_MWR\_rej = 3 - if the ice\_flag is 1 (ice contamination)
- flag\_MWR\_rej = 4 - based on statistical parameters, including median filters, function of the differences between MWR and model WTC, not only at the same measurements but also at neighbouring points (ice, land, rain or outlier detection).
- flag\_MWR\_rej = 5 - if the MWR WTC is  $\geq 0.05\text{m}$  or  $< 0.6\text{ m}$  (rain or ice contamination, or instrument failure)



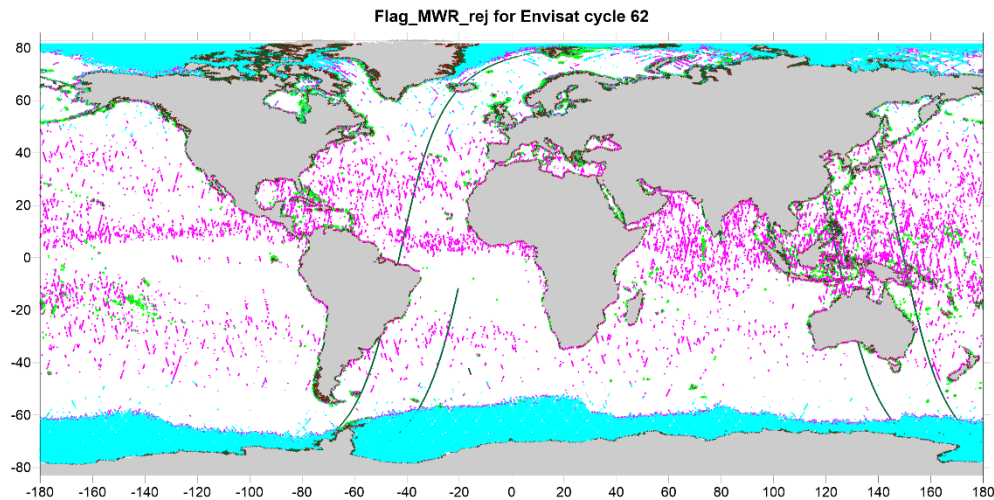
Figure 3.5 illustrates, for Envisat cycle 62 (top panel) and TOPEX/Poseidon cycle 443 (bottom panel), the points for which `flag_MWR_rej` is not zero, that is, the points where new values of the wet tropospheric correction are to be estimated. In addition to ocean points, to help on interpolation to higher data rates, the first land point of each track is also selected, provided it is within 50 km from the coastline (brown points in Figure 3.5). This figure demonstrates that the GPD is not merely a coastal algorithm, it is an ocean algorithm, including open-ocean, high latitudes and coastal zones.

### 2.3.4 Accuracy

Figure 3.6 illustrates the GPD formal error for Envisat cycle 62. To understand this figure, we recall that the GPD formal error is a function of the spatial and temporal distribution of the observations relative to the point of computation and also of the signal variance on the same point. The points for which there are no observations and the estimated value equals the model values adopted as first guess, were attributed a formal error of 1.5 cm. It can be observed that these points are mostly located in the polar regions, since in these regions the MWR observations are contaminated by ice.

The great majority of the points have a formal error within 1-2 cm. Considering that each output is a combination of all available observations, in the worst case, the estimation equals the first guess (model value).

Concerning the availability of valid MWR measurements, the worst cases take place when an isolated segment with all points having invalid MWR measurements occurs (usually when the track is parallel to the coastline, where a contaminated segment of several hundreds of kilometres length may occur. Due to the time difference between consecutive passes (100 minutes), in practice in the estimation of a given point only valid measurements from the same pass are used.





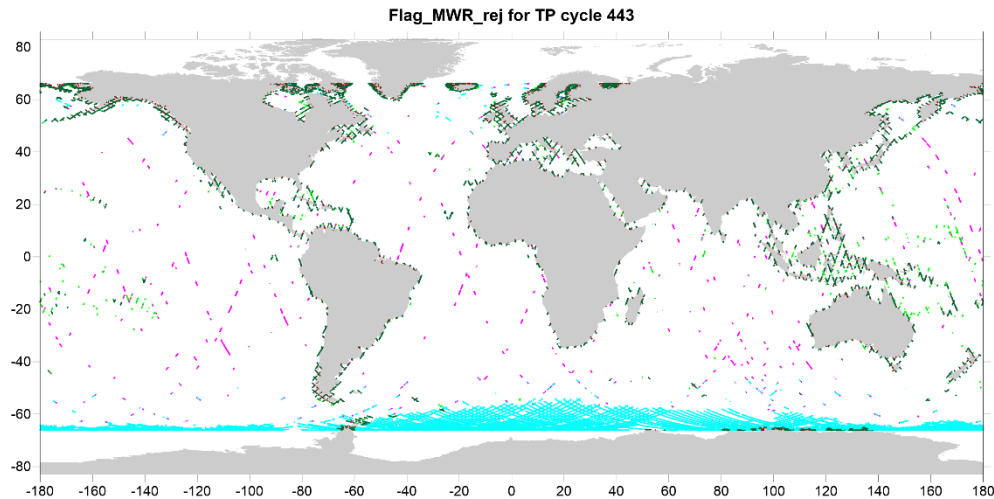


**Figure 3.5** - Location of Envisat cycle 62 (top) and TP cycle 443 (bottom) points selected for the GPD computation (points with  $\text{flag\_MWR\_rej} \neq 0$ ). Dark green: points with radiometer land flag set to 1; Light green: points with distance from coast less than a given threshold; Blue: points contaminated by ice; Pink: points rejected by outlier detection criteria or with the MWR WTC outside limits; Brown: land points near the coast (see text for details).

Comparing the error map with the map of the standard deviation of the WTC field shown in Figure 3.1 it can also be observed that the largest errors are also associated to regions of large field variance.

Considering the GNSS-derived path delays, various regions can be identified in Figure 3.6, e.g. around European and North American coastlines, where relatively dense networks of coastal stations can be found (c.f. Figure 3.1). However, there are many regions, particularly in the African coast, without available GNSS stations for distances of several hundreds of kilometres. In these regions the correction is solely based on valid MWR or SI-MWR measurements.

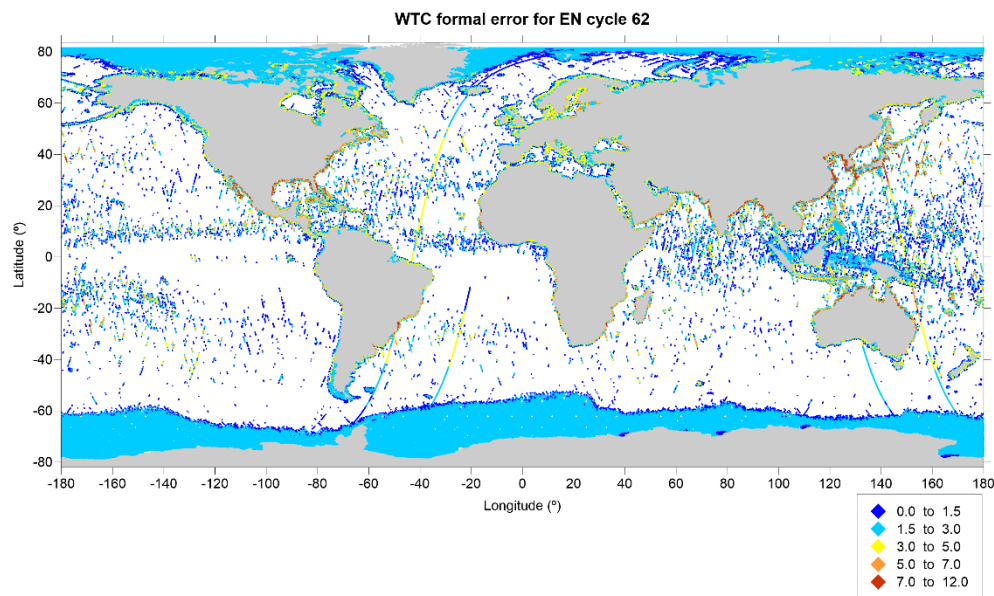


**Figure 3.6** - Formal error (in cm) of the GPD wet tropospheric correction for Envisat cycle 62.



## 2.3.5 References

- Bosser P, Bock O, Pelon J, Thom C (2007) An improved mean-gravity model for GPS hydrostatic delay calibration, *IEEE Geosci. Rem. Sens. Letters*, 4(1): 3-7.
- Bretherton FP, Davis RE, Fandry CB (1976) A technique for objective analysis and design of oceanographic experiment applied to MODE-73, *Deep-Sea Res.*, 23: 559-582.
- Brown, S. (2010) A novel near-land radiometer wet path-delay retrieval algorithm: Application to the Jason-2/OSTM advanced microwave radiometer. *IEEE Trans. Geosci. Remote Sens*, 48, 1986–1992.
- Davis JL, Herring TA, Shapiro II, Rogers AEE, Elgered G (1985) Geodesy by radio interferometry: effects of atmospheric modelling errors on estimates of baseline length. *Radio Sci* 20(6):1593-1607.
- Dee, D.P., Uppala, S.M., Simmons, A.J., Berrisford, P., Poli, P., Kobayashi, S., Andrae, U., Balmaseda, M.A., Balsamo, G., Bauer, P., et al (2011) The ERA-Interim reanalysis: Configuration and performance of the data assimilation system. *Q. J. R. Meteorol. Soc.*, 137, 553-597. ECMWF (2009) <http://www.ecmwf.int/products/catalogue/pseta.html>
- Fernandes, M.J.; Nunes, A.L.; Lázaro, C., (2013) Analysis and Inter-Calibration of Wet Path Delay Datasets to Compute the Wet Tropospheric Correction for CryoSat-2 over Ocean. *Remote Sens*. 2013, 5(10), 4977-5005, <http://www.mdpi.com/2072-4292/5/10/4977>
- Fernandes M. Joana, Clara Lázaro, Michaël Ablain, Nelson Pires.(2015) Improved wet path delays for all ESA and reference altimetric missions, *Remote Sensing of Environment*, Volume 169, November 2015, Pages 50-74, ISSN 0034-4257, <http://dx.doi.org/10.1016/j.rse.2015.07.023>.
- Fernandes MJ, Lázaro C, Nunes AL, Pires N, Bastos L, Mendes VB (2010) GNSS-derived Path Delay: an approach to compute the wet tropospheric correction for coastal altimetry. *IEEE Geosci. Rem. Sens Lett.*, 7(3): 596–600.
- Kouba J (2008) Implementation and testing of the gridded Vienna Mapping Function 1 (VMF1), *Journal of Geodesy*, 82:193-205. doi:10.1007/s00190-007-0170-0
- Leeuwenburgh O (2000) Covariance modelling for merging of multi-sensor ocean surface data, *Methods and Applications of Inversion*, Lect. Notes Earth Sci., vol. 92.
- Miller M, Buizza R, Haseler J, Hortal M, Janessen P, Untch A (2010) Increased resolution in the ECMWF deterministic and ensemble prediction systems. *ECMWF Newsletter* 124: 10-16.
- Schüler J (2001) On ground-based GPS tropospheric delay estimation, PhD Dissertation, Universität der Bundeswehr, München.
- Wentz, F., j. (2013) SSM/I Version-7 Calibration Report, RSS Technical Report 011012, Remote Sensing Systems, January 11, 2013.

## 2.4 ATBD-4: Sea state bias correction derived from the ALES algorithm

---

### 2.4.1 Selected altimeter standards

In the current stage of the project, the Sea State Bias correction is based on the output of Passaro et al. 2018 and the Sea Level CCI Bridging Phase. The selected standard will be called “20-Hz SSB” in this document.

### 2.4.2 Function

In the standard product, the SSB correction is derived using the methodology described in Gaspar et al. (2002) and Labroue et al. (2004) and updated in Tran et al. (2010). This methodology adopts a non-parametric estimation: a statistical technique (kernel smoothing) is used to solve a large system of linear equations based on the observations and on a set of weights. The result is a 2D map of the SSB against wind speed and SWH.





20-Hz SSB is the SSB correction derived by using the same 2D map from Tran et al. (2010) and obtained by courtesy of Ngan Tran from Collecte Localisation Satellites, but computed for each HF point using the HF wind speed and SWH estimations from ALES. The computation of the current SSB model is based on an empirical relationship between three retracked parameters. While part of it is due to the physics of the waves and will manifest itself at LF, the model contains also a relation that is due to the correlated errors in the estimation, which is performed at HF. Applying the SSB model at LF therefore means assuming that the error component of the sea level estimation related to the sea state exists only at long wavelengths, reducing its impact on the short-wavelength components.

### 2.4.3 Algorithm Definition

The application of 20-Hz SSB is based on the application of a look-up table, as explained in the previous section.

#### 2.4.3.1 Input Data

1. 2D map of the SSB against wind speed and SWH.
2. Range, SWH and sigma0 estimations from the ALES retracker

#### 2.4.3.2 Output Data

Sea State Bias correction at 20-Hz (40-Hz for Saral).

### 2.4.4 Accuracy

The current knowledge of the accuracy of 20Hz-SSB is based on the output of SL\_cci Bridging Phase. Further validation is not a task of the Algorithm Development in this project.

An overall performance analysis was performed globally on Jason-1 and Jason-2 by comparing crossover differences using the SGDR strategy (standard retracking + standard sea state bias correction) with the strategy followed in this project (ALES retracking + high rate sea state bias correction).

To obtain the 1-Hz sea surface heights we first subtract the estimated range from the orbital altitude and then we correct for pole tide, ocean tide, solid earth tide, geophysical effects (ionospheric delays, wet and dry tropospheric delays), dynamic atmosphere and sea state bias (using the original or the recomputed correction depending on the experiment). Finally, the median value of the screened 20-hz points within the 1-hz block is taken.

The 1-Hz points are used to perform a crossover analysis. This is a standard practice in altimetry and has been used in several publications as a key indicator of the data quality for altimetric missions. In order to reduce the impact of oceanic variability, crossovers are taken into consideration if the time lag between the two passes is shorter than 10 days. Crossovers are here defined as all the available 1-Hz points of two crossing tracks that are closer than 5 km.

Figure 4.1 shows, for each cycle of J1 and J2 reprocessed, the median of the STD of the crossover differences. For J1 in the global ocean, this value is 9.27 cm for SGDR and 7.99 cm for ALES; for J2 we have 9.86 cm for SGDR and 8.17 for ALES. This corresponds to a 30% improvement in variance, which is mostly due to the application of the Sea State Bias using the high-rate SWH and Wind estimations from ALES. Moreover, if we define as “outliers” the points in which the crossover differences exceed 50 cm or are not computable because the measurement is missing, we find out that in the coastal area within 20 km from the coast ALES has 6% less outliers than SGDR in Jason-1 and 10% less in Jason-2.

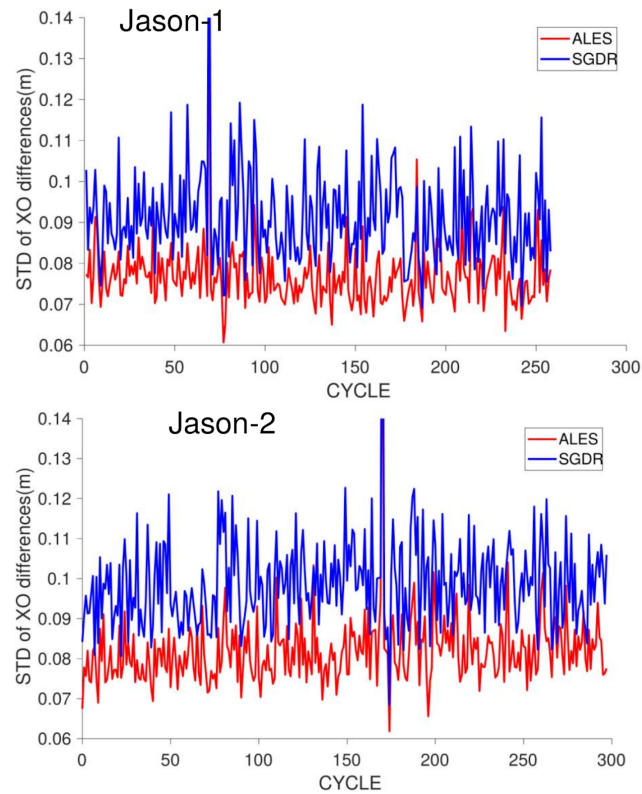


Figure 4.1: Global average by cycle of the Standard Deviation of the crossover differences for the SGDR dataset and the ALES dataset corrected for the high-rate Sea State Bias correction.

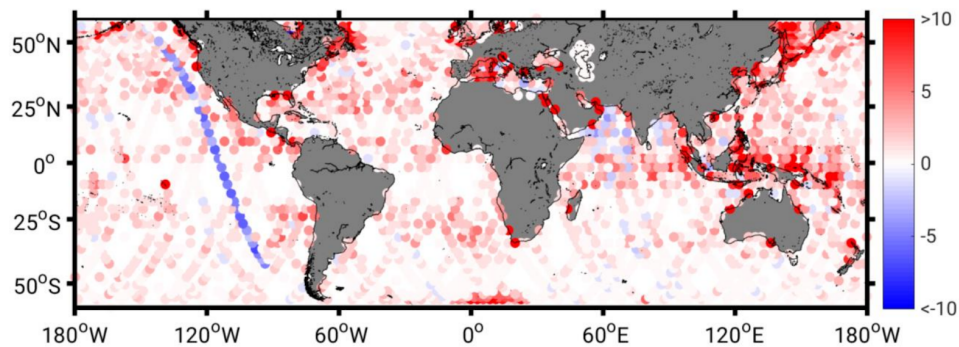


Figure 4.2: Difference between the number of outliers at crossover points in SGDR and ALES dataset corrected for the high-rate Sea State Bias correction.

### 2.4.5 References

- Gaspar, P., Labroue, S., Ogor, F., Lafitte, G., Marchal, L., Rafanel, M., 2002. Improving nonparametric estimates of the sea state bias in radar altimeter measurements of sea level. J. Atmos. Ocean. Technol. 19, 1690-1707.



- Labroue, S., Gaspar, P., Dorandeu, J., Zanife, O., Mertz, F., Vincent, P., Choquet, D., 2004. Nonparametric estimates of the sea state bias for the Jason-1 radar altimeter. *Mar.Geod.* 27, 453-481.
- Passaro M., Zulfikar Adlan N., Quartly G.D.: Improving the precision of sea level data from satellite altimetry with high-frequency and regional sea state bias corrections. *Remote Sensing of Environment*, 245-254, 10.1016/j.rse.2018.09.007, 2018
- Tran, N., Labroue, S., Philipps, S., Bronner, E., Picot, N., 2010a. Overview and update of the sea state bias corrections for the Jason-2, Jason-1 and TOPEX missions. *Mar.Geod.* 33, 348-362.

## 2.5 ATBD-5: The dual-frequency ionospheric correction filtered by X-TRACK

### 2.5.1 Selected altimeter standards

The ionospheric correction used in this project is the dual-frequency ionospheric correction provided in the GDR products distributed by the space agencies, edited, interpolated at 20-Hz for Jason, Envisat and SARAL missions and spatially filtered by the X-TRACK algorithm (described in details in Birol et al., 2016).

The strategy used in X-TRACK is to apply a two-step editing on the different corrective terms in order to recover the maximum number of meaningful sea level observations at the end of the processing. The first step consists in rejecting potential outliers through the analysis of each corrective term  $C_i$  used in the computation of the SLA data (Eq. 1.1, section 1)). Abrupt changes in consecutive correction values are assumed to be associated with errors. First, a threshold filter is applied along the satellite track (see section 2.5.2). In a second step, all the correction values are interpolated from a Bezier curve built from the edited data. The efficiency of this approach to recover significantly more coastal sea level data, compared to the standard procedure used by operational centers, was shown in different studies (Vignudelli et al., 2005, Durand et al., 2008, Birol et al., 2010 and Bouffard et al., 2011).

### 2.5.2 Function

The ionospheric correction calculated from the dual frequency altimeter measurements is noisy and has to be spatially filtered before it is removed from the altimeter range (Imel, 1994). A median absolute deviation (MAD) threshold filter is first applied to the original along-track record. This filter detects outliers efficiently since the median operator is much less influenced by extreme values than the standard deviation around the mean. The MAD value is computed using Equation 5.1. The ionospheric corrections values larger than  $3.5 \cdot \text{MAD}$  are considered as outliers and rejected.

$$\text{MAD} = \frac{1}{n} * \sum_{i=1}^n |x_i - R_{\text{med}}(X)| \quad \text{Eq. 5.1}$$

where  $n$  is the number of data in the record and  $R_{\text{med}}(X)$  is its running median value.

Figure 5.1 illustrates the corresponding editing process for the example of the cycle 10 of Jason-1 along the ground track 222 in the Mediterranean Sea. After the data cleaning, the along-track ionospheric corrections are smoothed by using a moving average filter. The number of points used in the moving average varies as a function of the measurement time. It is equal to 20 (i.e. ~140 km), except during the 0-6h time period when it is set to 25 (i.e. ~175 km), as the density of free electrons in the ionosphere is lower during this period of the day and induces smaller variations of the ionospheric path delay. In order to keep as much information as possible near the coast, a “mirror image” of the data time series is added onto the end of the series (i.e. near the coastline); this technique is appropriate because the ionospheric path delay exhibits little variation during the transit time between the open to the coastal ocean.

Finally, the edited and filtered ionospheric correction is interpolated at the 20-Hz times of the range measurements (not set at default values) using a Bezier curve which further low-pass filters the data and ensures a continuous slope of the signal in the case of data gaps (due to the presence of islands for example), as shown on Figure 5.1.

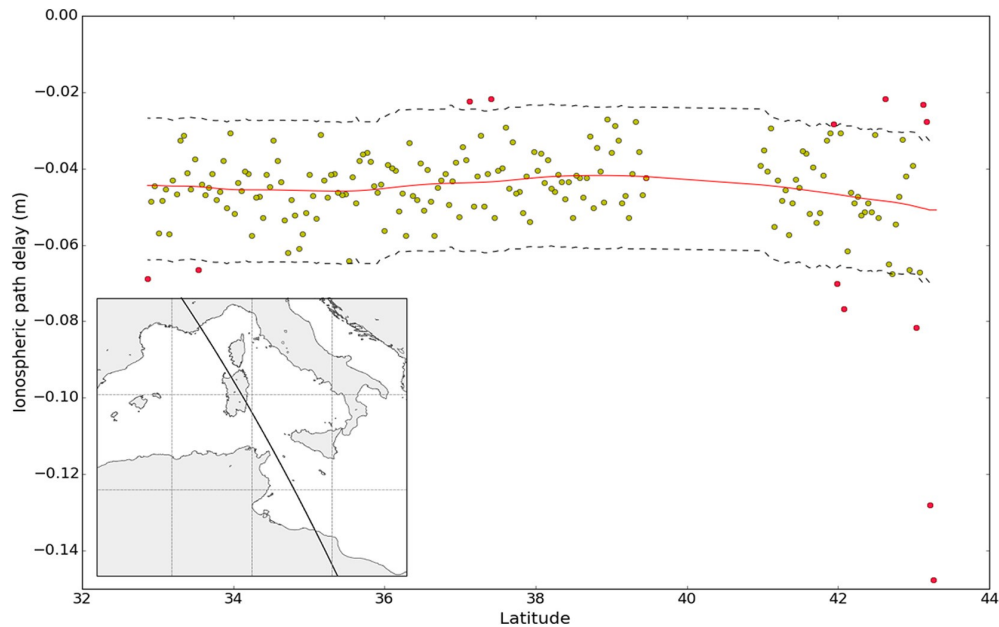


Fig. 5.1. Example of the ionospheric correction for the cycle 10 of Jason-1 along the ground track 222 in the Mediterranean Sea, before (yellow circles) and after (red line) X-TRACK edition and filtering. Red circles indicate the flagged values. The dash lines correspond to the MAD filter thresholds.

## 2.5.3 Algorithm Definition

### 2.5.3.1 Input Data

- Datation:
  - 1-Hz and 20-Hz altimeter time tag
- Location:
  - Latitude of the measurement (1 Hz and 20 Hz)
  - Longitude of the measurement (1 Hz and 20Hz)
- 1-Hz ionospheric correction derived from dual-frequency altimeter range measurements provided in the GDR products corresponding to the different altimeter missions.

### 2.5.3.2 Output Data

Ionospheric correction at 20-Hz edited and filtered in the along track direction by the X-TRACK algorithm (described in section 2.5.2).

## 2.5.4 Accuracy

The current knowledge of the accuracy of the dual-frequency ionospheric correction filtered by X-TRACK is based on the resulting sea level data.

An overall performance analysis was performed regionally on Topex/Poseidon, Jason-1 and Jason-2 by comparing the quantity of valid altimetry SLA (i.e., not flagged) provided by the X-TRACK



software and by the operational AVISO processing (an old version of the algorithm, called XTRACK 2011 is also represented on the Figure). This comparison is performed in the Mediterranean Sea. All Topex/Poseidon and Jason-1,2 1-Hz measurements are considered from March 1993 to May 2013 (a total of 747 cycles). Fig. 5.1 shows the number of valid SLA measurements over the 20-year period considered for all the tracks crossing the Mediterranean Sea for AVISO (in green), XTRACK 2011 (in red) and the version of X-TRACK used in this project (in black); the results are represented as a function of distance to the coast. The thick curves indicate the mean behavior of the three SLA datasets. The differences between the two X-TRACK and AVISO products are observed not only near the coasts but also offshore, with 20 cycles less on average for AVISO. For both versions of the X-TRACK products, the data availability is the same at distances larger than 20 km from the coast. It is larger for X-TRACK 2011 at distances shorter than 10 km (7% more cycles on average), whereas the availability of the X-TRACK 2016 data is slightly higher between 10 and 20 km. The standard deviations of the corresponding SLA time series have also been computed. They are also represented as a function of the distance to the coast (Fig. 5.1b). AVISO shows lower standard deviation values than X-TRACK everywhere (0.5 cm), probably due to a different spatial filter applied on the alongtrack SLA data and to a long wavelength error correction used to remove correlated noise due to orbit errors or uncertainties in geophysical corrections (not applied in X-TRACK processing). On Fig. 5.1b, we can also observe that in the X-TRACK version used in this project, compared to X-TRACK 2011, the signal variance is significantly reduced and much closer to AVISO at distances shorter than 40 km from the coast. This example clearly illustrates the benefit of the X-TRACK algorithm: compared to a classical post-processing chain, we obtain a larger number of coastal SLA, while keeping the same order of values in resulting SL statistics.

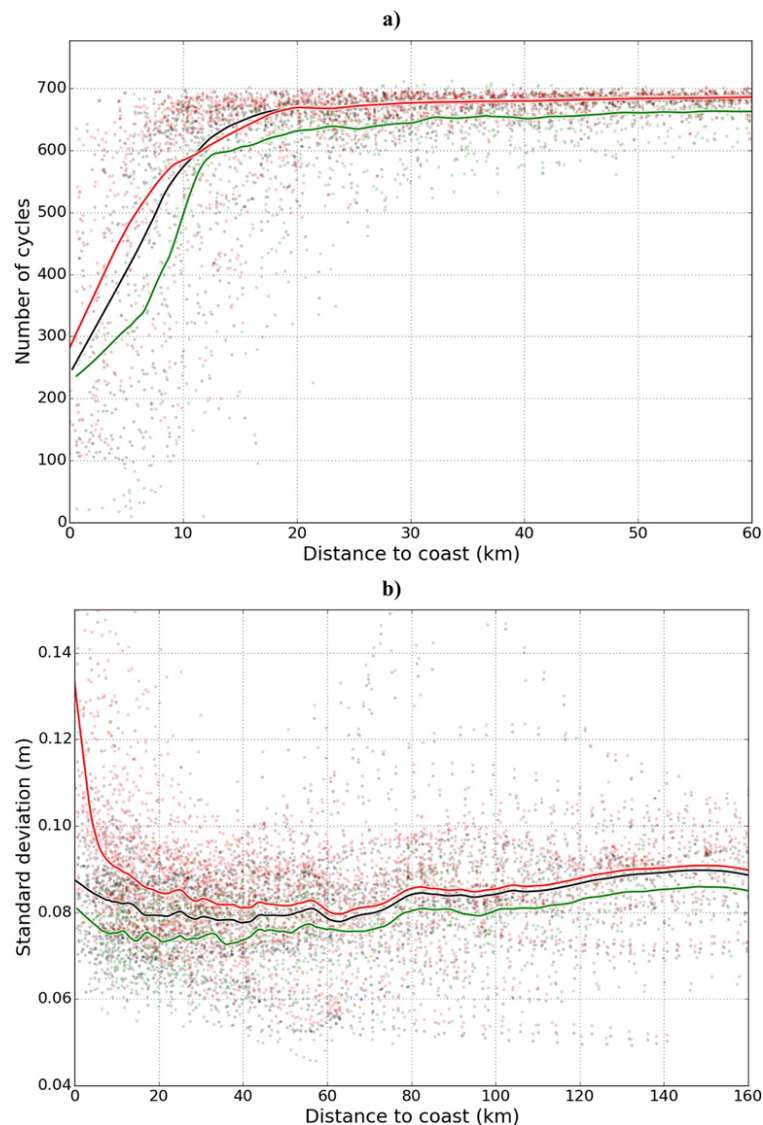






Figure 5.2 (a) Number of cycles available in the Mediterranean Sea from T/P and Jason1&2 missions over the period 1993-2013 in AVISO (in green), X-TRACK 2011 (in red) and X-TRACK 2016 (in black) products. (b) SLA standard deviation (in m) from T/P and Jason1&2 missions over the period 1993-2013 for AVISO (in green), X-TRACK 2011 (in red) and X-TRACK 2016 (in black). The results are represented as a function of the distance to the coast. The thick curves indicate the mean behavior of the three samples of SLA data.

## 2.5.5 References

- Birol, F., Cancet, M., Estournel, C., 2010. Aspects of the seasonal variability of the Northern Current (NW Mediterranean Sea) observed by altimetry. *J. Mar. Syst.* 81 (4), 297-311
- Birol F., N. Fuller, F. Lyard, M. Cancet, F. Niño, C. Delebecque, S. Fleury, F. Toubanc, A. Melet and M. Saraceno, F. Leger, 2016. Coastal applications from nadir altimetry: example of the X-TRACK regional products. *Advances in Space Research*, doi:10.1016/j.asr.2016.11.005.
- Bouffard, J., Roblou, L., Birol, F., Pascual, A., Fenoglio-Marc, L., Cancet, M., Morrow, R., Ménard, Y., 2011. Introduction and assessment of improved coastal altimetry strategies: case study over the northwestern Mediterranean Sea, chapter 12. In: Vignudelli, S., Kostianoy, A.G., Cipollini, P., Benveniste, J. (Eds.), *Coastal Altimetry*. Springer, Berlin, Heidelberg.
- Durand, F., Shankar, D., Birol, F., Shenoi, S.S.C., 2008. An algorithm to estimate coastal currents from satellite altimetry: a case study for the East India Coastal Current. *J. Oceanogr.* 64, 831-845.
- Imel, D., 1994. Evaluation of the Topex/Poseidon dual-frequency ionosphere correction. *J. Geophys. Res.* 99 (24), 895-906.
- Vignudelli, S., Cipollini, P., Roblou, L., Lyard, F., Gasparini, G.P., Manzella, G., Astraldi, M., 2005. Improved satellite altimetry in coastal systems: case study of the Corsica Channel (Mediterranean Sea). *Geophys. Res. Lett.* 32, L07608, doi:1029/2005GL22602.

## 2.6 ATBD-6: The high frequency fluctuations

### 2.6.1 Selected altimeter standards

Name	Description
Dynamical atmospheric correction derived from ERA-interim model	<p>The DAC correction is a combination of high frequencies of a barotropic model forced by pressure and wind (MOG2D model: <i>Carrère and Lyard 2003</i>; <i>SWT New Orleans 2002</i>) and the low frequencies of the IB.</p> <p>In the context of the Jason-1&amp;2 reference missions, the high frequencies have been defined to be the periods lower than 20 days, which correspond exactly to the Nyquist frequency of these altimeters' sampling.</p>

### 2.6.2 Function

To compute the high frequency fluctuations of the sea surface topography at the altimeter time tag and location from MOG2D model based on the ERA-Interim reanalysis computed by ECMWF.



## 2.6.3 Algorithm Definition

### 2.6.3.1 Input Data

- Datation:
  - 1-Hz altimeter time tag
- Location:
  - Latitude of the measurement (1 Hz)
  - Longitude of the measurement (1 Hz)
- MOG2D data: sum of the high frequency variability of the sea surface height and of the low frequency part of the inverted barometer effect (DAD) as computed in ERA-Interim.
- The data consists of two data files, 6 hours apart, surrounding the time of measurement (each file containing the parameter given on regular grid).

### 2.6.3.2 Output Data

- High frequency fluctuations of the sea surface topography (sum of the high frequency variability of the sea surface height and of the low frequency part of the inverted barometer effect) at the altimeter measurement time tag and location.

### 2.6.3.3 Mathematical statement

The Jason altimeters (10-day repeat cycle) deliver very accurate data sets (within 2 centimeter global error for T/P). However, for mesoscale circulation applications and satellite calibration campaigns, the HF ocean signal (periods less than 20 days for T/P), is aliased into the low frequency band (LF; periods larger than 20 days for T/P), and needs to be corrected from independent models at centimetric accuracy. The present HF tidal corrections have mainly reached this requirement, through the high-resolution hydrodynamic models. In contrast, the ocean response to meteorological forcing results poorly accounted if only the inverted barometer correction (IB) is applied. The MOG2D-G models the high frequency (HF) atmospheric forced variability of the global ocean with unprecedented accuracy. This hydrodynamic finite element (FE) model provides a global simulation of the ocean response to atmospheric wind and pressure forcing. MOG2D parameters (sum of the high frequency variability of the sea surface height and of the low frequency part of the inverted barometer effect) at the altimeter measurement are obtained by linear interpolation in time between two consecutive (6 hours apart) MOG2D model data files, and by bilinear interpolation in space from the four nearby model grid values.

The longitude of the altimeter measurement : Alt\_Lon\_Mean

The latitude of the altimeter measurement : Alt\_Lat\_Mean

The grid step in longitude : Lon\_Step

The grid step in latitude : Lat\_Step

The longitude of the first grid point : Lon-First

The latitude of the first grid point : Lat\_First

The number of grid points in longitude : Nb\_Lon

The number of grid points in latitude : Nb\_Lat

The cycling value in longitude : 360



The cycling value in latitude : 0

The truncation flag in longitude : 0

The truncation flag in latitude : 0

The indexes of the four grid points surrounding the measurement point: LL(lower Left), LR (lower right), UL (upper left), UR (upper right)

The weights of these four points:

The execution status

$$\left. \begin{aligned} V_{LL}(i, j) &= \text{MOG2D}(i, j(\text{lon}_L(i))) \\ V_{LR}(i, j) &= \text{MOG2D}(i, j(\text{lon}_R(i))) \\ V_{UL}(i, j) &= \text{MOG2D}(i, j(\text{lat}_L(i))) \\ V_{UR}(i, j) &= \text{MOG2D}(i, j(\text{lat}_U(i))) \end{aligned} \right\} \text{are the four nearby model values}$$

The parameter interpolated in space at altimeter measurement MOG2D\_Int\_Space

The number of valid cell points used by the interpolation (unused)

The execution status

## 2.6.4 Accuracy

The Dynamic Atmospheric Correction (DAC) is based on a global barotropic model (MOG2D), which has inherent errors due to the physic approximations, the grid size (ranging from 400 km in deep ocean to 20 km in coastal, shallow areas.), the forcing fields, the bathymetry errors, etc. Model outputs have been extensively compared to in situ data (tidal gauge, noted TGs; Carrère et Lyard 2003; Carrère, 2013): the model represents about 80 % of the high frequency variability and it allows reducing the TG variance by more than 50% if compared to the static IB; at low latitudes (between +/- 30°) the model is less efficient (gain of 10-20%) due to the dominance of the baroclinic signal, however signal is very weak in these regions. The residual variance of the temporal series corrected from the DAC correction, gives an estimation of the global error of this component, including: modelling errors (bathymetry, mesh resolution, forcing errors, etc.) and omissions errors, due to the lack of baroclinic physic for example. This global error is less than 10 % at high latitudes, and between 40-80 % at low latitudes; if looking at cm<sup>2</sup>, the residual variance is lower than 2 cm<sup>2</sup> in the intertropical region, where the variability at high frequencies is very weak, and about 5-10 cm<sup>2</sup> near the coasts (locally more than 100 cm<sup>2</sup>), where the high frequency variability is strong. Concerning barotropic velocities, the error distribution is mainly localized in coastal margin and in cape-like areas; in deeper regions this error is negligible.

## 2.6.5 References

- Loren Carrere and Florent Lyard, “Modeling the barotropic response of the global ocean to atmospheric wind and pressure forcing - comparison with observations”, Geophysical Research Letters, Vol. 30, NO 6, 1275, doi:10.1029/2002GL016473, 2003
- Carrere L., Faugère Y., Dupuy S., Ponte R. and Bronner E., “Comparisons to in situ data and estimation of errors in the Dynamic Atmospheric Correction”, OSTST Meeting 2013, Boulder, USA.





## 2.7 ATBD-7: The dry troposphere derived from ECMWF pressure fields

---

### 2.7.1 Selected altimeter standards

Name	Description	Missions
Dry troposphere derived from ECMWF pressure fields.	The dry troposphere (DT) is computed from ECMWF pressure fields.	Jason-1, Jason-2, Jason-3, Envisat and SARAL

### 2.7.2 Function

To compute at the altimeter time tag and location the dry tropospheric corrections (DTCs) due to gases of the troposphere from ECMWF pressure fields to which a model of S1 and S2 atmospheric pressure tides is added.

### 2.7.3 Algorithm Definition

#### 2.7.3.1 Input Data

- Datation:
  - 1-Hz altimeter time tag
- Location:
  - Latitude of the measurement (1 Hz)
  - Longitude of the measurement (1 Hz)
- Surface type:
  - Surface type (“open ocean or semi-enclosed seas”, “enclosed seas or lakes”, “continental ice”, or “land”)
- Meteorological data (DAD):
  - Meteorological data: surface pressure and mean sea surface pressure. For each of these 2 parameters, the data consist of two data files, 6 hours apart, bracketing the time of measurement (each file, excepted the mean sea surface pressure, contains the parameter given on the so-called Gaussian grid (quasi regular in latitude, non-regular in longitude).
  - Table providing the latitudes of the model grid points
  - Table providing the number of grid points in longitude for each model latitude
- Climatological pressure files (SAD)
  - The data consists of four data files, corresponding to 0h, 6h, 12h and 18h. Each file contains the climatological pressure referenced to the sea on a Cartesian grid, for each of the twelve months of the year.
- S1 and S2 tide grids of monthly means of global amplitude and phase
- Processing parameters (SAD)



### 2.7.3.2 Output Data

- Dry tropospheric correction:  $\delta h_{\text{dry}}$

### 2.7.3.3 Mathematical statement

The surface pressure and the mean sea surface pressure at the altimeter measurement are obtained by linear interpolation in time between two consecutive (6 hours apart) ECMWF model data files, and by bilinear interpolation in space from the four nearby model grid values (excepted for the mean sea surface pressure). The ECMWF model grid is quasi regular in latitude and non-regular in longitude (the number of grid points in longitude increases towards lower latitudes). If the surface type of the altimeter measurement is set to “open ocean or semi-enclosed seas”, only grid points having negative altitude are used in the interpolation (to avoid wrong tropospheric correction to be computed over ocean due to a grid point over high land altitude). If no such grid points with negative altitude are found, then the four grid points having positive altitude are used. If the altimeter measurement is set to “enclosed seas or lakes”, “continental ice”, or “land”, all grid points are used in the interpolation, whatever their altitude is.

The climatological S1 and S2 pressure (0h, 6h, 12h and 18h for each month) is then removed from the surface pressure, to correct from the aliasing of these signals due to the 6-hours sampling of the meteorological fields.

Finally, the dry tropospheric correction is derived from the surface pressure (climatological pressure removed) to which a model of S1 and S2 pressure variability (R D Ray and R M Ponte, 2003) is added.

Hereafter are detailed the mathematical statement used at Météo-France to compute the surface pressure map and the wet tropospheric correction map. The input data for computing these maps at Météo-France are the model surface pressure, and the specific humidity and temperature profiles from the vertical levels of the ECMWF model.

#### ***Definitions of the refractive index and of the dry tropospheric corrections***

The excess propagation path, also called path delay, induced by the neutral gases of the atmosphere between the backscattering surface and the satellite is given by:

$$\delta h = \int_{H_{\text{surf}}}^{H_{\text{sat}}} (n(z) - 1) dz \quad \text{Eq 7.4}$$

where  $n(z)$  is the index of refraction of air,  $H_{\text{surf}}$  and  $H_{\text{sat}}$  are respectively the altitudes of the surface and of the satellite above mean sea level.

The index of refraction is conveniently expressed in terms of the refractivity  $N(z)$ , defined as:

$$10^{-6} N(z) = n(z) - 1 \quad \text{Eq 7.5}$$

$N(z)$  is given by Bean and Dutton (1966):

$$N(z) = 77.6 \frac{P_d}{T} + 72 \frac{e}{T} + 3.75 \cdot 10^5 \frac{e}{T^2} \quad \text{Eq 7.6}$$



where  $P_d$  is the partial pressure of dry air in hPa (1 hPa = 100 Pa),  $e$  is the partial pressure of water vapor in hPa, and  $T$  is temperature in °K.

As the partial pressure of dry air is not easily measured, it is desirable to obtain an expression function of the total pressure of air. For deriving it, we have to consider that the dry air and the water vapor are ideal gases, i.e., they obey the Mariotte-Gay Lussac law:

$$\text{For dry air: } \frac{P_d}{\rho_d} = \frac{RT}{M_d} \quad \text{Eq 7.7}$$

$$\text{For water vapor: } \frac{e}{\rho_w} = \frac{RT}{M_w} \quad \text{Eq 7.8}$$

where  $\rho_d$  and  $\rho_w$  are the densities of dry air and water vapor respectively,  $M_d$  and  $M_w$  are the molar masses of dry air (28.9644  $10^{-3}$  kg) and water vapor (18.0153  $10^{-3}$  kg) respectively,  $R$  is the universal gas constant (8.31434 J.mole $^{-1}$ .K $^{-1}$ ).

Combining Eq 7.7, Eq 7.8 and Eq 7.6 leads to:

$$N(z) = 77.6 R \frac{\rho_d}{M_d} + 72 R \frac{\rho_w}{M_w} + 3.75 \cdot 10^5 \frac{e}{T^2} \quad \text{Eq 7.9}$$

The density of wet air is the sum of the densities of dry air and water vapor:  $\rho = \rho_d + \rho_w$  Eq 7.10

Introducing the density of wet air given by Eq 7.10 into Eq 7.9 leads to:

$$N(z) = 77.6 R \frac{\rho}{M_d} + (72 - 77.6 \frac{M_w}{M_d}) R \frac{\rho_w}{M_w} + 3.75 \cdot 10^5 \frac{e}{T^2} \quad \text{Eq 7.11}$$

Reintroducing Eq 7.8 into Eq 7.11 leads to the final expression of refractivity  $N(z)$ :

$$N(z) = 77.6 R \frac{\rho}{M_d} + (72 - 77.6 \frac{M_w}{M_d}) \frac{e}{T} + 3.75 \cdot 10^5 \frac{e}{T^2} \quad \text{Eq 7.12}$$

Combining this expression with Eq 7.4 and Eq 7.5 leads to the following equation for  $\delta h$ :

$$\delta h = 77.6 \cdot 10^{-6} \frac{R}{M_d} \int_{H_{surf}}^{H_{sat}} \rho dz + (72 - 77.6 \frac{M_w}{M_d}) 10^{-6} \int_{H_{surf}}^{H_{sat}} \frac{e}{T} dz + 3.75 \cdot 10^{-1} \int_{H_{surf}}^{H_{sat}} \frac{e}{T^2} dz \quad \text{Eq 7.13}$$

The first term is called the dry tropospheric correction  $\delta h_{dry}$ :

$$\delta h_{dry} = 77.6 \cdot 10^{-6} \frac{R}{M_d} \int_{H_{surf}}^{H_{sat}} \rho dz \quad \text{Eq 7.14}$$



The sum of the two remaining terms is called the wet tropospheric correction  $\delta h_{\text{wet}}$ :

$$\delta h_{\text{wet}} = (72 - 77.6 \frac{M_w}{M_d}) 10^{-6} \int_{H_{\text{surf}}}^{H_{\text{sat}}} \frac{e}{T} dz + 3.75 \cdot 10^{-1} \int_{H_{\text{surf}}}^{H_{\text{sat}}} \frac{e}{T^2} dz \quad \text{Eq 7.15}$$

Introducing the numerical values for  $M_d$  and  $M_w$  into Eq 7.15, and multiplying  $\delta h_{\text{wet}}$  by -1 to get a negative quantity to be added to the altimeter range, leads to the following equation for  $\delta h_{\text{wet}}$  in m:

$$\delta h_{\text{wet}} = -23.7 \cdot 10^{-6} \int_{H_{\text{surf}}}^{H_{\text{sat}}} \frac{e}{T} dz - 3.75 \cdot 10^{-1} \int_{H_{\text{surf}}}^{H_{\text{sat}}} \frac{e}{T^2} dz \quad \text{Eq 7.16}$$

### ***Calculation of the dry tropospheric correction as function of the surface pressure***

It is commonly assumed that the atmosphere is in hydrostatic equilibrium, i.e.  $g$  being the acceleration due to gravity:

$$\frac{dP}{dz} = -\rho g \quad \text{Eq 7.17}$$

Combining Eq 7.14 and Eq 7.17 leads to the following equation for  $\delta h_{\text{dry}}$ , where  $P_{\text{surf}}$  is the atmospheric pressure at the ground surface:

$$\delta h_{\text{dry}} = 77.6 \cdot 10^{-6} \frac{R}{M_d} \int_0^{P_{\text{surf}}} \frac{1}{g} dP \quad \text{Eq 7.18}$$

The dry tropospheric correction map given by Météo-France is computed from Eq 7.18.

The acceleration of gravity is a function of latitude and altitude. This function can be approximated by:

$$g = g_0 [1 - 0.0026 \cos(2\phi) - 0.00031z] \quad \text{Eq 7.19}$$

where  $\phi$  is the latitude,  $z$  is altitude in km, and  $g_0 = 9.80665 \text{ m/s}^2$

The variation of  $g$  with altitude is small and can be neglected by considering a mean value for  $g = 9.783 \text{ m/s}^2$  constant with altitude. This leads to the final expression for  $\delta h_{\text{dry}}$ :

$$\delta h_{\text{dry}} = -2.277 P_{\text{surf}} [1 + 0.0026 \cos(2\phi)] \quad \text{Eq 7.20}$$

Eq 7.20 is the expression obtained by Saastamoinen (1972), where  $P_{\text{surf}}$  is in hPa, and  $\delta h_{\text{dry}}$  is in mm and is set here with a negative sign to be added to the altimeter range. Computing the dry tropospheric correction from Eq 7.18 instead of from Eq 7.20 (i.e., taking into account the variation of  $g$  with altitude, as given by Eq 7.19), leads to differences below the 1-mm level in dry tropospheric correction (below the 0.5-mm level for latitudes less than  $50^\circ$ ).



*Note: In this algorithm, the dry tropospheric correction will be computed as described in Eq 7.20 but using a surface pressure which is the interpolated surface pressure  $P_{surf}$  from which the climatological pressure is removed (over the ocean only) and to which a model of  $S1$  and  $S2$  waves pressure variability (R D Ray and R M Ponte, 2003) is added.*

## 2.7.4 Accuracy

The accuracy of the dry tropospheric correction primarily depends on the accuracy of the surface pressure [Saastamoinen, 1972]. The best accuracy for surface pressure is achieved for analyzed fields. Typical errors vary from 1 hPa in northern Atlantic to more than 10 hPa in southern Pacific [Ray & Ponte, 2003]. A 1 hPa error on pressure translates to a 2 mm error on the dry tropospheric correction. The error introduced by space and time interpolation under the satellite track is probably small compared with the intrinsic inaccuracy of the surface pressure [Ray & Ponte, 2003]. For land surfaces, additional error is induced by the calculation of the surface pressure from the upper level pressure, due to assumptions on the mean virtual temperature of the atmospheric layer between the surface and the first upper level above the ground surface, and due to inaccurate knowledge of the TerrainBase digital elevation model (DEM) used for computing the altitude of the grid points above mean sea level. This additional error may be as large as the intrinsic error of the upper level pressure [Ray & Ponte, 2003].

## 2.7.5 References

- Bean, B. R., and E. J. Dutton, Radio Meteorology, U.S. NBS Monogr., 92, March 1966.
- Saastamoinen, J., 1972: Atmospheric correction for the troposphere and stratosphere in radio ranging of satellites, Geophys. Monogr., 15, American Geophysical Union, Washington D.C.
- R D Ray and R M Ponte, Barometric tides from ECMWF operational analyses, Annales Geophysicae, 21: 1897-1910, 2003.

## 2.8 ATBD-8: The ocean tide height (including long period equilibrium ocean tide) and load tide height

---

The geocentric (elastic) ocean tide is the sum of the ocean tide and the load tide. It is a major contributor to sea level variability and it is observed by altimeters on board satellites.

### 2.8.1 Selected altimeter standards

Name	Description	Mission applicability
FES2014 tide model	The tide model computes the tide correction at satellites location and date using FES2014 wave tide files of amplitude and phase.	Jason-1, Jason-2, Jason-3, Envisat and SARAL

### 2.8.2 Function

- To compute the ocean tide from the FES2014 harmonic components algorithm (using FES2014 model), using the diurnal and semidiurnal components as well as some non-linear and long-period ones. To add the height of the equilibrium long period ocean tide. The ocean tide height does not include the load tide height.



- To provide the ocean tide (including long period ocean tide) in output.
- To compute the height of the tidal loading induced by the ocean tide from GOT4v8ac harmonic components.
- To provide the load tide in output. To add the ocean tide (including long period ocean tide) and the load tide to compute the geocentric (elastic) ocean tide.

### 2.8.3 Algorithm Definition

#### 2.8.3.1 Input Data

- Datation:
  - Altimeter time tag
- Location:
  - Latitude of the measurement
  - Longitude of the measurement
- Height of the equilibrium long period ocean tide: long period tides are gravitational tides, typically with amplitudes of a few centimeters or less and periods longer than a day, generated by changes in the Earth's orientation relative to the Sun and Moon. The equilibrium tide height is defined to be proportional to the gradient of the tide potential, assuming a rigid spheric Earth covered by a thin water layer with no inertia, nor viscosity.
- Harmonic coefficients maps of the principal tidal waves (SAD)
- Load tide harmonic coefficients maps of the principal tidal waves (SAD)
- The frequencies and the phases at 0h on 1/1/1900 of five astronomical variables, respectively the mean longitude of the moon, the mean longitude of the sun, the mean longitude of the lunar perigee, the negative of the mean longitude of the lunar ascending node and the mean longitude of the solar perigee
- The frequencies of the 34 tidal waves
- The admittance parameters

#### 2.8.3.2 Output Data

- Ocean tide height including long period ocean tide (solution 1 = FES2014 harmonic components)
- Height of the tidal loading (solution 1 = GOT4.8ac harmonic components)

#### 2.8.3.3 Mathematical statement

- The height of the ocean tide is the sum of N tidal constituents  $h_i$  (Schureman, 1958):

$$h_i = F_i [A_i(\phi, \mu) \cdot \cos(\psi_i) + B_i(\phi, \mu) \cdot \sin(\psi_i)] \quad (i=1, N) \quad \text{Eq 8.21}$$



with:  $\psi_i = \sigma_i \cdot t + X_i + U_i$   
 $F_i$  is the tidal coefficient of amplitude nodal correction (depends only on the altimeter time)  
 $U_i$  is the tidal phase nodal correction (depends only on the altimeter time)  
 $X_i$  is the tidal astronomical argument (depends only on the altimeter time)  
 $\sigma_i$  is the tidal frequency  
 $t$ ,  $\phi$  and  $\mu$  are respectively the altimeter time tag, latitude and longitude

$A_i(\phi, \mu)$  and  $B_i(\phi, \mu)$  are harmonic coefficients bi-linearly interpolated at the altimeter location  $(\phi, \mu)$  from the input harmonic coefficients map given by the GOT4.8 model (Ray, 2013). Harmonic coefficients A and B are tidal amplitude x cos(phase) and tidal amplitude x sin(phase) respectively.

- The height of the tidal loading is the sum of N constituents  $h_i$ :

$$h_i = F_i [C_i(\phi, \mu) \cdot \cos(\psi_i) + D_i(\phi, \mu) \cdot \sin(\psi_i)] \quad (i=1, N) \quad \text{Eq 8.22}$$

$C_i(\phi, \mu)$  and  $D_i(\phi, \mu)$  are harmonic coefficients bi-linearly interpolated at the altimeter location  $(\phi, \mu)$  from the input harmonic coefficients map. This map has been computed from Ray (1999).  $N = 26$  tidal constituents were used. Among these 26 tidal constituents, 8 principal ones were given in input amplitudes and phases maps, the 18 remaining ones were computed by admittance from the principal constituents 1 to 8, using admittance coefficients.

Two additional principal waves (S1 and M4) are taken into account, leading thus to a total number of 28 components.

- The height of the geocentric (elastic) ocean tide height is the sum of the height of the ocean tide, including the height of the equilibrium long period ocean tide (input of the algorithm), and the height of the tidal loading.

## 2.8.4 Accuracy

A typical value for deep ocean tide model error is a 1 cm error (Lyard et al. 2006; Ray, 2011; Carrère et al, 2012; Cancet et al.2012). This error will likely be reduced while improving the in situ comparison dataset (work being done by R. Ray, personal communication 2013). In shallow water this error is higher due to higher modelling and omission errors: the modelling error includes bathymetry error, mesh resolution, and hydrodynamic approximations error, and the omission error is due to the lack of non-linear waves in most of models. The global rms difference with a 179-shallow-waters database is about 10 cm (Ray, 2011), but it can reach several tens of cm if compared to a more complete and coastal database (Cancet et al, 2012; Carrère et al. 2012): between 18-36 cm error for M2 wave if compared to a coastal dataset, and between 20-50 cm for a shelf database (extended dataset if compared to R. Ray's one).

## 2.8.5 References

- Cancet, M. and J. Lamouroux (2012), Modèle de marée FES2012 - tâche 4, NOV-3918-NT-12304\_v2.0.pdf, 10/2012.
- Carrère L., F. Lyard, M. Cancet, A. Guillot, L. Roblou (2012), FES 2012: a new global tidal model taking advantage of nearly 20 years of altimetry, Proceedings of 20 years of Altimetry, Venice 2012.
- Lyard, F., et al. (2006), Modeling the global ocean tides: a modern insight from FES2004, Ocean Dynamics, 56, 394-415.



- Ray, R.D. (2013), Precise comparisons of bottom-pressure and altimetric ocean tides, J. Geophys. Res. Oceans, 118, 4570-4584, doi:10.1002/jgrc.20336.
- Ray R.D., Egbert G.D., Erofeeva S.Y. (2011) Tide Predictions in Shelf and Coastal Waters: Status and Prospects. In: Vignudelli S., Kostianoy A., Cipollini P., Benveniste J. (eds) Coastal Altimetry. Springer, Berlin, Heidelberg, doi: 10.1007/978-3-642-12796-0\_8
- Ray, R. D. (1999), A global ocean tide model from Topex/Poseidon altimetry: GOT99.2, NASA Tech.Memo., 209478.
- Schureman, P. (1958), Manual of harmonic analysis and prediction of tides, US Department of Commerce, Special Publication No. 98.

## 2.9 ATBD-9: Mean Sea Surface Height derived from the X-TRACK algorithm

### 2.9.1 Selected altimeter standards

The mean sea surface height used in this project is computed by the X-TRACK algorithm (described in details in Birol et al., 2016).

### 2.9.2 Function

Once the corrected SSHs are derived using Eq. 9.1, for each satellite track, a 20-Hz mean sea surface height (MSS) is computed along a nominal ground track. 20-Hz cells are first defined all along the theoretical altimeter pass (as in Figure 9.1). In each cell, the barycenters of the locations of the original 20-Hz measurements are computed (black stars in Figure 9.1) and the nominal ground track is defined as the pass linking all these barycenters (mean cell coordinates in Figure 9.1) which are called the reference points.

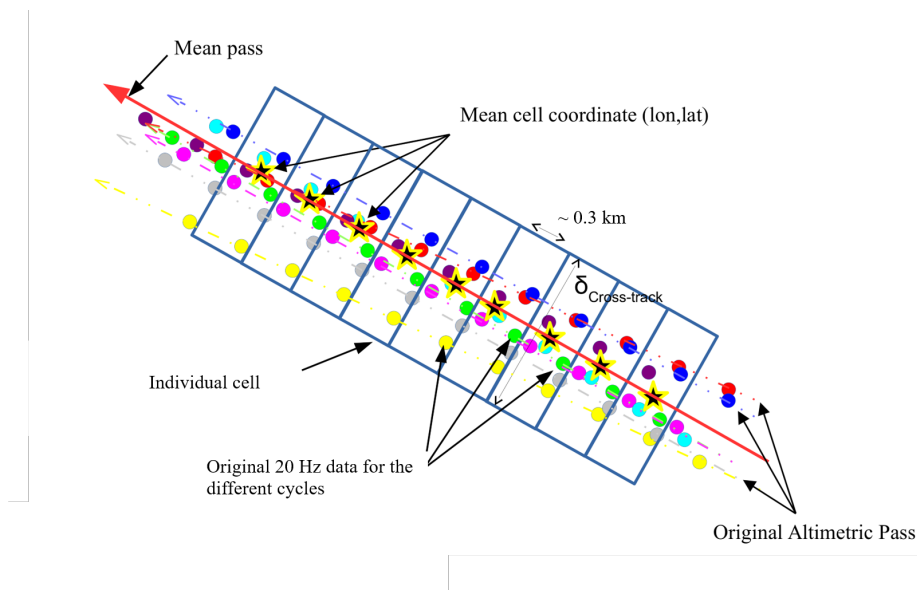


Figure 9.1: Illustration of the normalized pass definition for a particular pass. The original data are represented by different colours (one colour per cycle). The pass is divided in cells in the along track direction and all the data are ordered in their corresponding cell (one value per cycle in each cell). For each cell, the mean cell coordinate (black stars) is then defined as the mean of the coordinates of all the original data (corresponding to all the cycles considered).





$$Corrected\ SSH = Orbit - Range - \sum_{i=0}^N C_i \quad \text{Eq 9.1}$$

where Orbit corresponds to the distance between the satellite and the ellipsoid, Range is the distance measured by the altimeter between the satellite and the sea surface, and  $\sum_{i=0}^N C_i$  is the sum of all the altimetry corrections detailed above.

In a second time, the data are resampled at the reference points along the nominal track: the SLA time series are obtained by subtracting to the corrected SSH data both the MSS at the closest reference point ( $MSS_0$ ) and the MSS difference between the closest reference point ( $x_0, y_0$ ) and the actual location of the altimeter observation ( $x, y$ ):

$$SLA(x, y) = Corrected\ SSH - MSS_0 - \Delta MSS(x, y, x_0, y_0) \quad \text{Eq 9.2}$$

$\Delta MSS(x, y, x_0, y_0)$  accounts for the cross track and along-track gradient of the corrected SSH values. At the first order they correspond to the geoid variations which can be large at short wavelengths, especially in coastal areas.

The SSH variations around the reference points are modelled as the quadratic equation expressed below:

$$Corrected\ SSH(x, y) = MSS_0 + a_1 dx + a_2 dy + a_3 dx * dy + a_4 dx^2 + a_5 dy^2 \quad \text{Eq 9.3}$$

with: dx is the difference in longitude between the original altimetry measurement and the closest reference point, dy is the difference in latitude between the original altimetry measurement and the closest reference point.

In Eq. 9.3, the parameters  $MSS_0$ ,  $a_i (i = 1, 2, 3, 4, 5)$  are computed by inversion of the Corrected SSH data.

## 2.9.3 Algorithm Definition

### 2.9.3.1 Input Data

- Datation:
  - 20-Hz altimeter time tag
- Location:
  - Latitude of the 20-Hz measurement
  - Longitude of the 20-Hz measurement
  - 20-Hz corrected SSH (using the orbit, range and list of corrections described above, e.g. ATBD1 to ATBD8).

### 2.9.3.2 Output Data

- 20-Hz alongtrack MSS computed with X-TRACK
- 20-Hz SLA

## 2.9.4 Accuracy

This procedure is important since it was found that in coastal areas, where the surface topography gradients are large, inaccurate MSS leads to significant errors in SLAs (Vignudelli et al., 2005).



However, as for the ionospheric correction, the current knowledge of the accuracy the MSS computed by X-TRACK is based on the resulting sea level data: see section 2.5.4.

## 2.9.5 References

- Birol F., N. Fuller, F. Lyard, M. Cancet, F. Niño, C. Delebecque, S. Fleury, F. Toubanc, A. Melet and M. Saraceno, F. Leger, 2016. Coastal applications from nadir altimetry: example of the X-TRACK regional products. *Advances in Space Research*, doi:10.1016/j.asr.2016.11.005.
- Vignudelli, S., Cipollini, P., Roblou, L., Lyard, F., Gasparini, G.P., Manzella, G., Astraldi, M., 2005. Improved satellite altimetry in coastal systems: case study of the Corsica Channel (Mediterranean Sea). *Geophys. Res. Let.* 32, L07608, doi:1029/2005GL22602.

End of the document